Dating growth strata and basin fill by combining $^{26}Al/^{10}Be$ burial dating and magnetostratigraphy: Constraining active deformation in the Pamir–Tian Shan convergence zone, NW China

Jessica Ann Thompson Jobe[1,2], Tao Li[3,4], Bodo Bookhagen[5,6], Jie Chen[3], and Douglas Burbank[1]
[1]DEPARTMENT OF EARTH SCIENCE, UNIVERSITY OF CALIFORNIA–SANTA BARBARA, SANTA BARBARA, CALIFORNIA 93106, USA
[2]INSTITUTE OF TECTONIC STUDIES, DEPARTMENT OF GEOLOGICAL SCIENCES, THE UNIVERSITY OF TEXAS EL PASO, EL PASO, TEXAS 79968, USA
[3]STATE KEY LABORATORY OF EARTHQUAKE DYNAMICS, INSTITUTE OF GEOLOGY, CHINA EARTHQUAKE ADMINISTRATION, BEIJING 100029, CHINA
[4]GUANGDONG PROVINCIAL KEY LABORATORY OF GEODYNAMICS AND GEOHAZARDS, SCHOOL OF EARTH SCIENCE AND ENGINEERING, SUN YAT-SEN UNIVERSITY, GUANGZHOU 510275, CHINA
[5]DEPARTMENT OF GEOGRAPHY, UNIVERSITY OF CALIFORNIA–SANTA BARBARA, SANTA BARBARA, CALIFORNIA 93106, USA
[6]INSTITUTE OF EARTH AND ENVIRONMENTAL SCIENCES, UNIVERSITY OF POTSDAM, 14476 POTSDAM, GERMANY

ABSTRACT

Cosmogenic burial dating enables dating of coarse-grained, Pliocene–Pleistocene sedimentary units that are typically difficult to date with traditional methods, such as magnetostratigraphy. In the actively deforming western Tarim Basin in NW China, Pliocene–Pleistocene conglomerates were dated at eight sites, integrating $^{26}Al/^{10}Be$ burial dating with previously published magnetostratigraphic sections. These samples were collected from growth strata on the flanks of growing folds and from sedimentary units beneath active faults to place timing constraints on the initiation of deformation of structures within the basin and on shortening rates on active faults. These new basin-fill and growth-strata ages document the late Neogene and Quaternary growth of the Pamir and Tian Shan orogens between >5 and 1 Ma and delineate the eastward propagation of deformation at rates up to 115 km/m.y. and basinward growth of both mountain belts at rates up to 12 km/m.y.

INTRODUCTION

Sedimentary basins adjacent to and within growing orogens provide key insights into the deformational and erosional history of the orogen. Many basins contain syntectonic growth strata that provide a direct means to determine the timing of tectonic deformation (Riba, 1976; Suppe et al., 1992; Talling et al., 1995; Heermance et al., 2008). Among the various dating methods, magnetostratigraphy is commonly the most suitable tool for dating thick syntectonic continental sediments (Butler et al., 1977; Ensley and Verosub, 1982; Burbank et al., 1992; Beamud et al., 2011; Gunderson et al., 2014). In some regions, however, the initiation of uplift of adjacent ranges leads to deposition of coarse-grained material, such as conglomerates, for which the use of magnetostratigraphy is not feasible due to a lack of fine-grained interbeds, or where magnetostratigraphic correlation to the geomagnetic polarity time scale (GPTS) is ambiguous due to unconformities, poor biostratigraphic control, a lack of dateable volcanic ashes that provide radiometric constraints, or the brevity of the observed magnetostratigraphic record (e.g., the piggyback basin in Heermance et al., 2007). Thus, dating of conglomeratic sedimentary basin fills and/or syntectonic growth strata remains a challenge.

Cosmogenic radionuclide burial dating, which relies on the decay of multiple in situ cosmogenic radionuclides, is a technique used to date

sediments that range in age from 0.3 to 6 Ma (Granger et al., 1997; Granger and Muzikar, 2001; Wolkowinsky and Granger, 2004; Craddock et al., 2010; Balco and Rovey, 2010; Vermeesch et al., 2010; Kong et al., 2011; Ciampalini et al., 2015). These radionuclides, or isotopes, are produced in quartz as rocks exhume and erode in catchment areas. The isotopes decay at rates dictated by their different half-lives. After fluvial transport, deposition, and burial in the downstream basin, the samples are commonly buried deep enough that they are effectively shielded from cosmic radiation such that the production of the isotopes becomes negligible, and the decreasing ratio of $^{26}Al/^{10}Be$ can be used to calculate the time since burial (or deposition). This technique has typically been used to date sediments in caves that have a simple burial history (Granger et al., 1997; Stock et al., 2004; Liu et al., 2015), but it has also recently been applied to dating deltaic (Ciampalini et al., 2015), lacustrine (Davis et al., 2011), littoral (Gunderson et al., 2014), and fluvial sediments (Erlanger et al., 2012; Matmon et al., 2012; Balco et al., 2013; Zhang et al., 2014; Tu et al., 2015; McPhillips et al., 2016; Tofelde et al., 2017) that may have experienced more complicated exposure-burial histories (Wittmann et al., 2011).

The Pamir and Tian Shan orogens in the western Tarim Basin in NW China (Fig. 1) formed as a delayed response to the Indo-Eurasian collision. These two east-west–trending orogens now impinge on each other and are gradually deforming and closing the western Tarim Basin, creating a series of faults and folds that disrupt the foreland (Chen et al., 2002; Scharer et al., 2004; Heermance et al., 2008; Li et al., 2012; Thompson Jobe et al.,

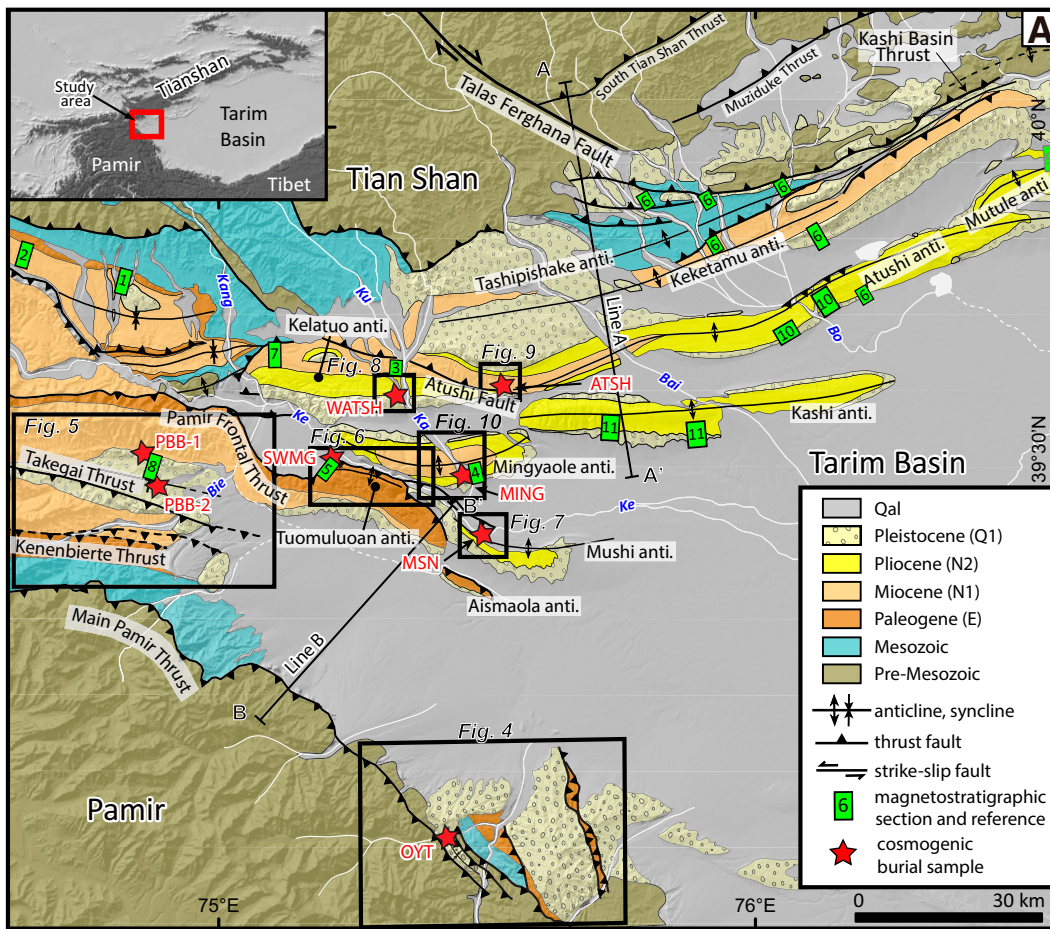Jessica A. Thompson Jobe ⓘ http://orcid.org/0000-0001-5574-4523

Figure 1. (A) Simplified geologic map of the western Tarim Basin. Inset map marks location in Central Asia. Map is modified from Li et al. (2015a) and Thompson Jobe et al. (2017). Magnetostratigraphic sections discussed in text include: 1—Tang et al. (2015); 2—Chen et al. (2015); 3—Liu et al. (2017); 4—Chen et al. (2005); 5—Li et al. (2012); 6—Heermance et al. (2007); 7—Qiao et al. (2017); 8—Thompson et al. (2015); 9—Qiao et al. (2016); located ~10 km to east of shown location); 10—Chen et al. (2002); 11—Chen et al. (2007). Bie—Bieertuokuoyi River; Ke—Kezilesu River; Kang—Kangsu River; Bai—Baishikeremu River; Ka—Kalanggouluke River; Bo—Boguzi River; Ku—Kuzigongsu River. (B) Interpretation of seismic reflection data across the southern Tian Shan, line A, modified from Heermance et al. (2008) and Thompson Jobe et al. (2017). (C) Interpretation of seismic reflection data across the northeastern Pamir, line B, from Chen et al. (2010), Cheng et al. (2016), and Thompson Jobe et al. (2017). AA—Atushi anticline; AF—Atushi fault; KA—Kashi anticline; KBT—Kashi Basin thrust; KKA—Keketamu anticline; KT—Kenenbierte thrust; MPT—Main Pamir thrust; Mz—Mesozoic; N2-Q—Pliocene–Pleistocene; N-Q—Neogene–Quaternary; PFT—Pamir Frontal thrust; PreMz—pre-Mesozoic; STSF—South Tian Shan fault; TT—Takegai thrust; TA—Tashipishake anticline.
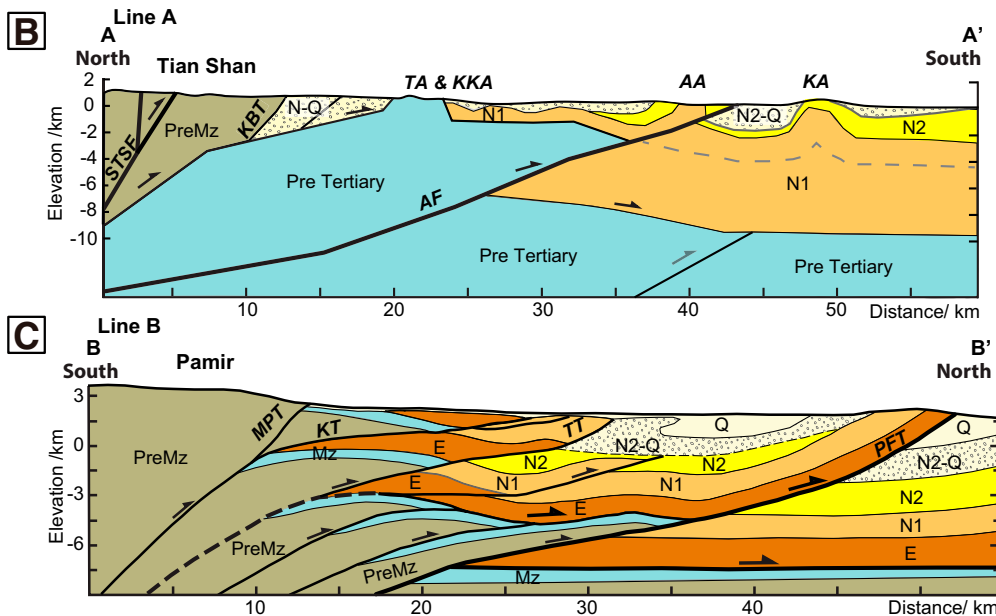
2017). To determine the onset of deformation of individual structures in the foreland, we used [10]Be and [26]Al produced in quartz to date the spatially extensive, conglomeratic, Pliocene–Pleistocene Xiyu Formation. These strata exhibit clear relationships to faults and growth strata on the flanks of growing folds. We used shielded samples from both caves and narrow, deeply incised canyons, such that postdepositional nuclide production during exhumation was minimized or could be constrained. Where feasible, we combined our burial ages with published magnetostratigraphic sections to place further constraints on the deposition of the basins and the deformation of nearby structures (e.g., Gunderson et al., 2014). When integrated with previous studies, our results document both the late Neogene, basinward growth of the Pamir and Tian Shan orogens, as well as the eastward propagation of deformation due to the Pamir–Tian Shan collision. Furthermore, this study demonstrates an innovative way to date coarse-grained strata and structures on the margins of growing orogens.

GEOLOGIC SETTING

Tectonic History

The Pamir and Tian Shan orogens formed as a result of the Indo-Eurasian collision (Fig. 1). These two orogens are obliquely converging, zippering closed the western Tarim Basin trapped between them. Earlier during the Cenozoic, the northern Pamir indented northward ~300 km relative to stable Eurasia (Burtman and Molnar, 1993). This indentation was accommodated by movement along a series of sinistral and dextral strike-slip faults on the eastern and western margins (Sobel et al., 2011), thrusting on the northern margin (Strecker et al., 1995; Coutand et al., 2002), and intracontinental subduction of the Eurasian plate beneath the Pamir along a southward-dipping subduction zone (Negredo et al., 2007; Schneider et al., 2013), in addition to crustal shortening and significant crustal thickening within the Pamir (Burtman and Molnar, 1993).

Low-temperature thermochronology from the interior and margins of the Pamir and Tian Shan indicates exhumation and shortening initiated in the Eocene or Oligocene and continues to the present (Sobel and Dumitru, 1997; Sobel et al., 2006; Heermance et al., 2007, 2008; Amidon and Hynek, 2010; Schmidt et al., 2011; Sobel et al., 2011, 2013; Stearns et al., 2015; Rutte et al., 2017). Along the northern margin of the Pamir, in the Alai valley, shortening began during the Oligocene–Miocene and continues to the present (Strecker et al., 1995; Coutand et al., 2002; Zubovich et al., 2016). Farther west, where the Pamir and Tian Shan are already juxtaposed, the collision began as late as the Miocene–Pliocene (Pavlis et al., 1997).

Deformation on the northeastern margin of the Pamir has been focused on a series of imbricate thrust faults that have propagated into the foreland since the Miocene (Sobel and Dumitru, 1997; Sobel et al., 2011, 2013; Li et al., 2012; Thompson et al., 2015; Cheng et al., 2016; Wang et al., 2016). Based on detrital low-temperature thermochronology, the Main Pamir thrust (MPT), the southernmost fault at the edge of the Pamir, initiated 25–18 Ma, although the slip rate may have slowed during the late Miocene or Pliocene (Sobel and Dumitru, 1997; Sobel et al., 2011). Low seismic activity, geodetic convergence rates (Zubovich et al., 2010; Li et al., 2012), and interferometric synthetic aperture radar (InSAR) signals (Bufe et al., 2017a) indicate low modern slip rates (<1 mm/yr) on the MPT on the Pamir's northeastern margin. Frontal faults of the Pamir thrust system initiated during the late Miocene (Thompson et al., 2015), with most of the recent deformation focused on the Mushi anticline and the Pamir Frontal thrust (PFT) since ca. 350 ka (Li et al., 2012, 2013; Thompson Jobe et al., 2017). Geodetic and geologic slip rates and InSAR data reveal the PFT is shortening at a rate of 6–8 mm/yr (Zubovich et al., 2010; Li et al., 2012, 2013; Ischuk et al., 2013).

Similar to the Pamir, deformation on the southern margin of the Tian Shan has been focused on imbricate thrust faults and related folds, but these structures have propagated southward into the foreland since the Miocene (Fig. 1B; Heermance et al., 2008). Low-temperature thermochronology dates the onset of exhumation on the margins of the Tian Shan to ca. 20 Ma (Sobel et al., 2006), with accelerated and pulsed deformation migrating southward since the middle Miocene (Heermance et al., 2008). Deformation continued to step southward during the Miocene through the Quaternary (Heermance et al., 2008; Bufe et al., 2017a; Thompson Jobe et al., 2017). Currently, deformation on the southern front of the Tian Shan is focused in several subparallel detachment or fault-propagation folds within the Kashi-Atushi fold-and-thrust belt (Fig. 1) at rates >2–3 mm/yr (Scharer et al., 2004; Chen et al., 2007; Heermance et al., 2008; Gao et al., 2013; Bufe et al., 2017a, 2017b; Li et al., 2012, 2013, 2015a, 2015b; Thompson Jobe et al., 2017).

Stratigraphy of the Western Tarim Basin

The western Tarim Basin contains up to 9 km of Cenozoic strata (Heermance et al., 2007; Bally et al., 1986), which unconformably rest on top of Paleozoic or Mesozoic bedrock (Fig. 2). At the base of the Cenozoic section, Paleogene strata include mudstones, siltstones, sandstones, and evaporites, which serve as a regional detachment surface transferring shortening into the foreland (Cheng et al., 2016; Wang et al., 2016). Neogene strata include the fluvial, eolian, and lacustrine strata of the Miocene Wuqia Group and Pliocene Atushi Formation (Heermance et al., 2007). At the top of the basin stratigraphy is the time-transgressive Xiyu Formation, a thick sequence of conglomerates interbedded with discontinuous sandstones (Heermance et al., 2007; Charreau et al., 2009; Thompson et al., 2015). All growth strata within the basin have thus far been observed in the Xiyu Formation and the very upper Atushi Formation (Chen et al., 2002, 2005, 2007; Heermance et al., 2007; Thompson et al., 2015).

[26]Al/[10]Be COSMOGENIC BURIAL DATING

Background

Burial dating relies on the decay of two radionuclides, [10]Be and [26]Al, which are produced through spallation, negative muon capture, and fast muon interactions in quartz during exhumation on hillslopes, transport in rivers, and near-surface storage as sediment (Fig. 3; Lal, 1991). Although the production rates of [10]Be and [26]Al vary with latitude and altitude, [26]Al is always produced ~6.75 times faster than [10]Be (Nishiizumi et al., 1989; Granger and Muzikar, 2001). In the absence of significant sedimentary recycling, this production rate determines the initial inherited nuclide ratio of the sediment. Importantly, this ratio is independent of the erosion rate or any short-term transport history. Once the sediment is buried and no longer exposed to cosmic rays, [10]Be and [26]Al decay at rates equal to their half-lives (1.38 m.y. and 717 k.y., respectively; Norris et al., 1983; Chmeleff et al., 2010). Thus, the ratio of [26]Al/[10]Be can be used to calculate the age since burial, assuming that the samples have been sufficiently shielded once buried (Granger and Muzikar, 2001). Two nuclides must be used, because at least two unknowns are embedded in the history of the sediment: the initial concentration of the isotopes (which is a function of the source-area erosion rate and elevation and of the preburial exposure time), and the duration the sediment has been buried.

The concentrations of [10]Be and [26]Al vary with time according to Equations 1 and 2 (Granger and Muzikar, 2001):

$$N_{Al}(t) = N_{Al}(0) e^{-t/\tau_{Al}} + P_{Al}(z)\tau_{Al}\left(1 - e^{-t/\tau_{Al}}\right), \quad (1)$$
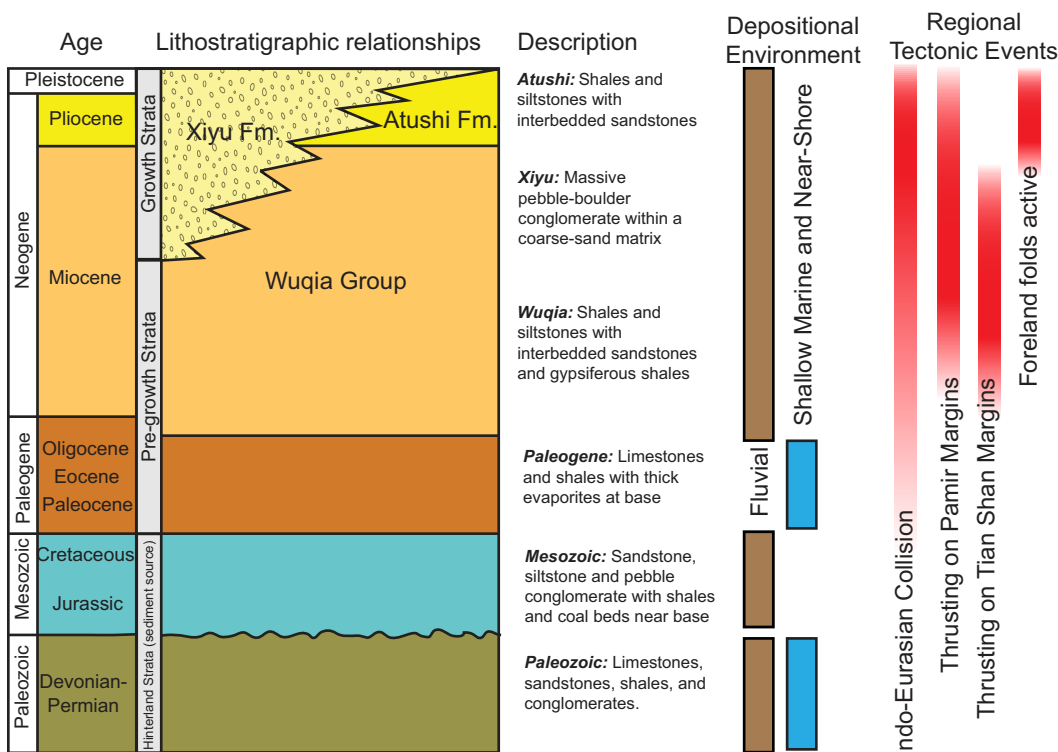
Figure 2. Regional stratigraphy, depositional environments, and tectonic events of the western Tarim Basin. Stratigraphic descriptions and interpreted depositional environments are from Carroll et al. (1995); Heermance et al. (2007); and Thompson et al. (2015). Timing of regional tectonic events is from Sobel and Dumitru (1997); Sobel et al. (2006); Chen et al. (2002); Heermance et al. (2008); and Thompson et al. (2015). Note growth and pregrowth strata, and the units that form the hanging walls of major thrusts in the hinterlands.

$$N_{Be}(t) = N_{Be}(0)e^{-t/\tau_{Be}} + P_{Be}(z)\tau_{Be}\left(1 - e^{-t/\tau_{Be}}\right), \qquad (2)$$

where $N(t)$ is the concentration at the time of sampling, the first term on the right side is the decay of the initial concentration (with t as the burial age), and the second term on the right side is postburial production. P_{Al} or P_{Be} is the production of ^{26}Al or ^{10}Be, respectively, at a constant given depth (z), and it includes spallogenic and muogenic production. N_{Al} is the concentration of ^{26}Al, N_{Be} is the concentration of ^{10}Be, τ_{Al} is the mean life of ^{26}Al (1.021 ± 0.024 m.y.; Nishiizumi, 2004), and τ_{Be} is the mean life of ^{10}Be (2.005 ± 0.020 m.y.; Chmeleff et al., 2010). In cases where a sample has been well shielded for its entire postdepositional history, the second term is commonly low and can be ignored. However, if shielding has not been sufficient to prevent significant postburial production, the production rates at depth can be calculated as follows:

$$P_{Al}(z) = A_0 e^{-z/\Lambda_0} + A_1 e^{-z/\Lambda_1} + A_2 e^{-z/\Lambda_2} + A_3 e^{-z/\Lambda_3}, \qquad (3)$$

and

$$P_{Be}(z) = B_0 e^{-z/\Lambda_0} + B_1 e^{-z/\Lambda_1} + B_2 e^{-z/\Lambda_2} + B_3 e^{-z/\Lambda_3}, \qquad (4)$$

where z is the depth, ρ is the density (2.65 g/cm³), $\Lambda_0 \approx 160/\rho$ cm, $\Lambda_1 \approx 738/\rho$ cm, $\Lambda_2 \approx 2688/\rho$ cm, and $\Lambda_3 \approx 4360/\rho$ cm (Granger and Muzikar, 2001). Estimates for production rates at sea level and at high latitude are $A_0 \approx 31.1$, $A_1 \approx 0.72$, $A_2 \approx 0.16$, $A_3 \approx 0.19$, $B_0 \approx 4.63$, $B_1 \approx 0.09$, $B_2 \approx 0.02$, and $B_3 \approx 0.02$ (Granger and Muzikar, 2001), in units of atoms per year per gram of quartz, which are then scaled to the field area from the sea-level, high-latitude (SLHL) values of 31.1 and 4.63 atoms/g/yr for ^{26}Al and ^{10}Be, respectively (Granger and Muzikar, 2001; Balco et al., 2008). The values are scaled to the field sites using scaling schemes that make a latitude- and altitude-dependent correction for spallogenic production and an atmospheric pressure–dependent correction for all muogenic production reactions (Stone, 2000).

The initial concentration of the quartz $N(0)$ from an eroding landform can be approximated as:

$$N_{Al}(0) = \frac{A_0}{\frac{1}{\tau_{Al}} + \frac{E}{\Lambda_0}} + \frac{A_1}{\frac{1}{\tau_{Al}} + \frac{E}{\Lambda_1}} + \frac{A_2}{\frac{1}{\tau_{Al}} + \frac{E}{\Lambda_2}} + \frac{A_3}{\frac{1}{\tau_{Al}} + \frac{E}{\Lambda_3}}, \qquad (5)$$

and

$$N_{Be}(0) = \frac{B_0}{\frac{1}{\tau_{Be}} + \frac{E}{\Lambda_0}} + \frac{B_1}{\frac{1}{\tau_{Be}} + \frac{E}{\Lambda_1}} + \frac{B_2}{\frac{1}{\tau_{Be}} + \frac{E}{\Lambda_2}} + \frac{B_3}{\frac{1}{\tau_{Be}} + \frac{E}{\Lambda_3}}, \qquad (6)$$

where E is the erosion rate within the source area, and Λ is the attenuation length. By combining Equations 1–6, a system of equations can be formed that are solved simultaneously for both the erosion rate and the time of burial (Granger and Muzikar, 2001).

Preburial History

The preburial history of the sediments impacts the initial $^{26}Al/^{10}Be$ ratio. For example, if the sediments were eroded from older foreland basin sediments that experienced a prior period of erosion, deposition, and burial, without being buried long enough to decay to ~0, the initial $^{26}Al/^{10}Be$ ratio will be lower than the assumed 6.75:1 ratio. Thus, the derived burial ages are considered maximum ages only.

Postburial Production

Ideally, the sediment experienced a simple exposure history: It was eroded from a source area, having accumulated some concentration of ^{10}Be and ^{26}Al in quartz as it was exhumed on the hillslopes, transported almost instantaneously through the fluvial system (relative to the burial time),
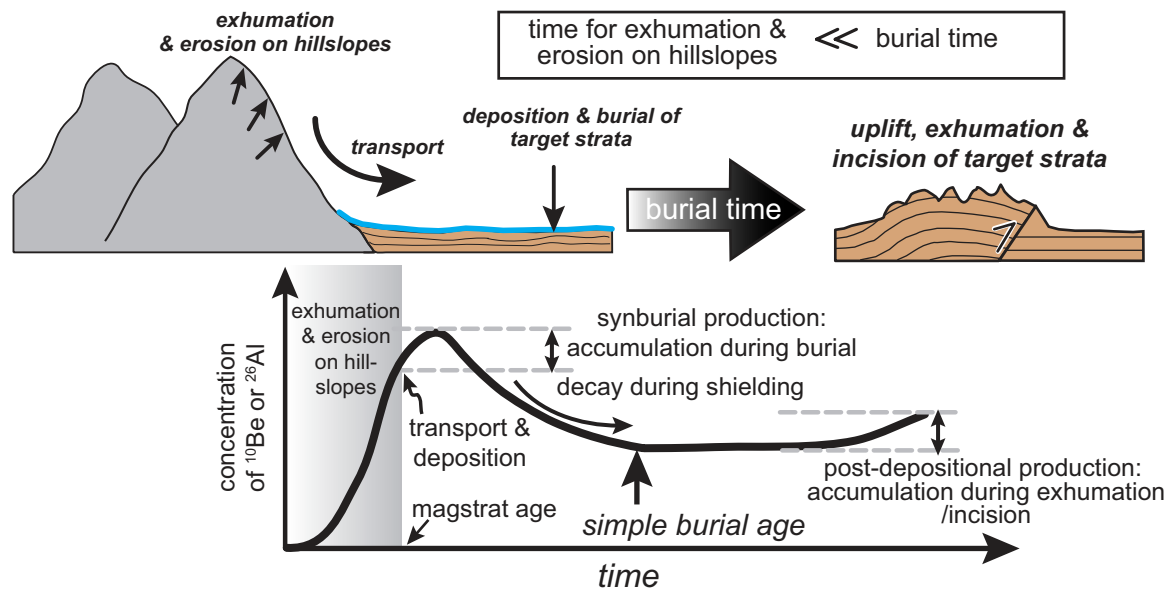
Figure 3. Schematic diagram of the erosion, transport, and burial history of sediments in a basin. Top: Quartz grains are exhumed and eroded on hillslopes in the source area, transported through the fluvial system, and deposited and buried in the adjacent basin. After some length of time that is much greater (at least an order of magnitude) than the previous steps, the sediments may be exhumed, uplifted, and incised such that sampling is feasible. Bottom: Schematic chart illustrating the concentration of ^{10}Be or ^{26}Al through time. The concentration increases during initial exhumation and erosion on the hillslopes. The sediments accumulate a minor additional concentration during burial, termed synburial production. Once buried, the concentrations decrease as ^{10}Be and ^{26}Al decay during shielding. If the sediments are sampled following rapid exhumation, a simple burial age has occurred. If exhumation is slow, such that considerable new nuclide production occurs, concentrations of ^{10}Be and ^{26}Al will have increased during exhumation such that postdepositional production should be accounted for in the burial age calculations. Abbreviation: magstrat age—magnetostratigraphic age. Axes are schematic and not to scale.

deposited, and rapidly buried to a depth (>30 m) where postburial production effectively ceases, and then it was exhumed shortly before sampling. A sample with an assumed simple burial and exhumation history will yield what is called the simple burial age. Unfortunately, a simple transport, burial, and exhumation history, and the assumption that the sample has remained well shielded since its final deposition are commonly not true in tectonically active areas, and in these cases, both postburial production and a prolonged transport history (i.e., transient storage in the catchment) can have a significant effect on the burial ages (Puchol et al., 2017). In contrast to the common application of burial dating to cave sediments, which are well shielded since deposition, the sediments in basins may experience prolonged exposure during burial and reexposure during subsequent deformation (Matmon et al., 2014; Ciampalini et al., 2015; Puchol et al., 2017).

Postburial production, which is the production of ^{26}Al and ^{10}Be after the initial exhumation, erosion, and transport on hillslopes, increases the concentrations and ratio of ^{26}Al and ^{10}Be, resulting in an apparently younger age. Two common situations can be constrained and accounted for in postburial production: (1) production during initial slow burial of the sediment in the basin, hereafter referred to as synburial production, and (2) production due to reduced shielding resulting from exhumation and/or incision during the late Quaternary.

Synburial production may occur after the sediment is initially deposited, but prior to burial deep enough (>30 m) that production effectively ceases (Fig. 3). This situation may arise when sediments are slowly deposited in a basin (30–100 m/m.y.; Zhang et al., 2014). In this case, thousands to hundreds of thousands of years may pass before the target strata are buried deeper than 30 m. The faster the sediment-accumulation rates are, the lower the synburial production is. Given that sediment-accumulation rates of the Pliocene–Pleistocene Xiyu Formation in the Kashi Basin range

from 400 to 1000 m/m.y. (and are usually closer to 800–1000 m/m.y.; Chen et al., 2002; Heermance et al., 2007, 2008; Li et al., 2012; Thompson et al., 2015), we assert that it is a reasonable assumption that the sediments were rapidly buried to a sufficient depth such that synburial production is insignificant. At a minimum, it would take only ~5000 yr to bury the sediment to a depth >5 m (assuming ~1000 m/m.y.), and only ~30,000 yr to bury the sediment to >30 m, such that even muogenic production nearly ceases (Granger et al., 1997; Granger and Muzikar, 2001). On the other hand, if sediment-accumulation rates were as slow as 400 m/m.y., it would take ~75,000 yr to pass this same production-rate threshold. Whereas synburial production appears to have little effect on burial ages in the western Tarim Basin (<5%), its effect should be assessed in different regions with low (<100 m/m.y.) sediment-accumulation rates.

Postburial production also occurs during exhumation and incision of the landscape, as occurred during the late Quaternary, hereafter termed postdepositional production. Within the detection limits of ^{10}Be and ^{26}Al, postdepositional production may be minimal in rapidly exhuming regions and can commonly be constrained by dating related geomorphic surfaces (Matmon et al., 2014; Puchol et al., 2017). In the western Tarim Basin, typical rock uplift rates of folds in the foreland range from ~1 to 5 mm/yr (Bufe et al., 2017a). At these fast rock uplift rates, additional production of ^{10}Be and ^{26}Al during exhumation and uplift is likely minimal, because the rock spends a relatively short amount of time in the cosmogenic isotope production depths. However, prolonged exposure near the surface following uplift and incision may lead to additional production of ^{10}Be and ^{26}Al that may, depending on the length of exposure, bias the signal to a higher ^{26}Al/^{10}Be ratio and hence a younger apparent burial age. Existing dated terraces in the western Tarim provide timing constraints on recent exposure for calculating this type of postdepositional production (Li et

al., 2012, 2013, 2015b; Thompson Jobe et al., 2017; Bufe et al., 2017b; Thompson et al., 2018).

Sample Collection, Processing, and Age Calculations

Growth strata form during the deposition of sediment on the flanks of growing structures (Suppe et al., 1992). At eight sites in the western Tarim Basin, we described and interpreted stratal geometries adjacent to folds as growth strata that could be confidently related to the deformation of nearby faults and folds (Fig. 1). At these locations, the bedding is conformable, except at the edges of the folds, where slight angular unconformities and tapering bed thicknesses were observed. The transition from conformable beds to progressive unconformities is interpreted to represent a change from stable to tectonically active conditions (Riba, 1976; Poblet et al., 1997), where the fold may begin to emerge above the land surface. We based our interpretations of growth strata on three criteria, where at least two criteria were directly observed or measured at each site: (1) decreasing dips up section toward the flanks of the fold, (2) thickening of beds away from the anticline, and (3) common minor angular unconformities between beds near the edges of the fold. Thus, dating the base of the growth strata defines a youngest initiation age for fold growth. In addition, previously published subsurface data on some of the folds support our interpretation of growth strata (Chen et al., 2007; Heermance et al., 2008; Chen et al., 2010; Cheng et al., 2016).

We collected samples from in situ coarse sand lenses and conglomerate beds at the back of shielded small caves and under overhangs (Table 1) from the base of units we interpreted to be growth strata. From conglomerate beds, we separated the sand matrix from the clasts, and we only analyzed the sand. For each sample, we amalgamated ~5 kg of sand from a single bed or lens collected over a horizontal distance of ~1 m.

To minimize production during incision and exhumation after initial deposition, we tried to sample sites that were well shielded by at least 30 m of rock. When that was not possible, we corrected for postdepositional production during the time since the rocks were shielded by less than 30 m, as constrained by optically stimulated luminescence (OSL) and/or

^{10}Be cosmogenic depth-profile dating of overlying fluvial terraces, with several key assumptions, described below.

The samples were processed following standard procedures at the Cosmogenic Isotope Laboratory at the University of California, Santa Barbara (Bookhagen and Strecker, 2012). The purity of quartz was verified by inductively coupled plasma–mass spectrometry (ICP-MS) measurements of Al, which yielded <100 ppm (< 40 mg) in all samples (Table 2). The ^{10}Be and ^{26}Al measurements were made at Lawrence Livermore National Laboratory and at the Purdue Rare Isotope Measurement facility (PRIME) using the 07KNSTD standard (Table 2; GSA Data Repository Table DR2[1]).

We calculated the burial ages following Equations 1–6 (Granger and Muzikar, 2001), using the sea-level, high-latitude (SLHL) production rates listed above and scaled to the sample sites following the scaling scheme of Lal (1991) and Stone (2000). Our calculations relied on three simplifying assumptions: (1) We assumed a rock density of 2.65 g/cm^3 in all calculations. Within the crystalline, metamorphic, and compacted sedimentary rocks, this density is a reasonable assumption. Yet, for late Quaternary fluvial gravels or initial sediment deposition and burial within a basin, which likely have a lower density, this assumption will introduce some uncertainty. For well-shielded, rapidly buried or exhumed samples (>30 m), variations in density have little effect on the production rate and resulting burial ages (<5%; Thompson, 2013). (2) Production rates were scaled to the SLHL values using the present-day latitude and elevation of the samples. Importantly, the initial ratio of ^{26}Al and ^{10}Be in the samples is more important than the independent production rates of ^{26}Al and ^{10}Be. (3) All uncertainties in the reported burial age reflect only the analytical uncertainties from the accelerator mass spectrometer (AMS) measurements of the concentrations of ^{10}Be and ^{26}Al and uncertainties in the mean lives. We did not propagate uncertainties in the production rates. Nonetheless, production rates may have uncertainties up to 10% (Balco et al., 2008). In this study, the uncertainties in the production rates and density variations are small compared to the analytical uncertainties of the Al measurements, and, therefore, we propose it is reasonable to ignore them.

For at least four of our samples, late Quaternary river incision reduced the shielding, and postdepositional nuclide production likely had an effect

TABLE 1. SITE CHARACTERISTICS FOR BURIAL SAMPLES

| Sample | Related fault or fold | Location | | Elevation (m) | Depth (m) | Width (m) | Shielding* | Description |
		Latitude (°N)	Longitude (°E)					
MING	Mingyaole anticline	39.4853	75.4774	1630	56	3	0.169	Small overhang in recently incised valley; terraces above valley date to ca. 15 ka
PBB-1	PFT, TT	39.5290	74.8370	2589	200+	0.5	N.D.	Narrow overhang from within a deep incised valley
PBB-2	PFT, TT	39.4921	74.8515	2695	100+	16	0.159	Small cave with a larger bowl-shaped cave
WATSH	Kelatuo anticline	39.5978	75.3431	1998	46	12	N.D.	Narrow overhang from within a deep incised valley
MSN	Mushi anticline	39.4248	75.5042	1785	12	3	N.D.	Small overhang in recently incised valley; terraces above are estimated to date to ca. 40–30 ka; only depth shielding included in postdepositional production (no topographic shielding collected)
OYT	MPT	38.9671	75.4331	1998	100+	2.0	N.D.	Narrow overhang within a deep incised valley
ATSH	Atushi fault & Atushi anticline	39.6050	75.5207	1937	64	2.3	0.668	Small overhang in recently incised valley; possibly shielded by only 8 m during end of late Quaternary
SWMG	PFT	39.5150	75.2144	1725	30	4.5	0.456	Small cave in a recently incised valley; terraces ~50 m above valley date to ca. 15 ka

Note: Depth refers to the depth of incision of the sample collection site below a surface, commonly a terrace. Width refers to the width of the overhang or cave from which the sample was collected, which was used to calculate a nominal shielding. MPT—Main Pamir thrust; PFT—Pamir Frontal thrust; TT—Takegai thrust; N.D.—no data.
*Includes topographic and depth shielding during postdepositional nuclide production, for samples where a postdepositional production correction was necessary.

TABLE 2. ^{26}AL AND ^{10}Be COSMOGENIC DATA AND AGES FOR BURIAL SAMPLES

Sample	Mass quartz (g)	^{10}Be/^{9}Be*,† (×10^{-14})	^{9}Be carrier* (mg)	^{10}Be† (×10^4 atoms g^{-1})	^{26}Al/^{27}Al§,# (×10^{-14})	^{27}Al** (mg)	^{26}Al# (×10^4 atoms g^{-1})	^{26}Al/^{10}Be ratio††	Simple ^{26}Al/^{10}Be age†† (Ma)	Corrected ^{26}Al/^{10}Be age††,§§ (Ma)
MING	142.4	56.6 ± 1.4	0.220	5.84 ± 0.15	7.90 ± 3.6	22.46	27.8 ± 12.7	4.8 $^{+1.9}/_{-2.1}$	0.9 $^{+1.1}/_{-0.7}$	0.9 $^{+1.1}/_{-0.7}$
PBB-1	116.0	7.6 ± 0.6	0.230	1.00 ± 0.08	0.81 ± 0.6	10.25	1.6 ± 1.27	1.6 $^{+1.1}/_{-1.0}$	2.9 $^{+1.7}/_{-1.1}$	N.D.
PBB-2	144.7	12.47 ± 0.4	0.220	1.27 ± 0.04	0.4 ± 1.3	21.52	3.32 ± 1.71	2.6 $^{+1.4}/_{-1.3}$	1.9 $^{+1.4}/_{-1.9}$	N.D.
WATSH	164.7	29.0 ± 0.6	0.210	2.47 ± 0.05	>0.1 ± 28.6	27.53	0.37 ± 107	0.2 ± 12400	>5	N.D.
MSN	169.7	45.4 ± 2.4	0.232	4.1 ± 0.22	1.8 ± 5.6	38.54	9.12 ± 28.2	2.2 $^{+2.3}/_{-1.3}$	2.0 $^{+2.0}/_{-1.2}$	2.1 $^{+2.1}/_{-1.2}$
OYT	117.3	2.19 ± 0.4	0.253	0.31 ± 0.05	0.1 ± 2.3	25.27	0.48 ± 10.9	1.5 $^{+1.5}/_{-1.1}$	3.3 $^{+1.8}/_{-1.8}$	N.D.
ATSH	149.0	16.5 ± 0.4	0.230	1.70 ± 0.04	0.4 ± 1.5	29.6	1.77 ± 6.51	1.1 $^{+5.0}/_{-0.1}$	3.5 $^{+2.1}/_{-1.2}$	3.8 $^{+2.1}/_{-1.3}$
SWMG	136.7	20.1 ± 0.4	0.220	2.16 ± 0.05	1.90 ± 1.4	20.17	6.25 ± 4.57	2.9 $^{+2.2}/_{-1.6}$	1.6 $^{+1.8}/_{-0.9}$	1.7 $^{+1.7}/_{-0.8}$

Note: ^{26}Al/^{27}Al measurements for samples PBB-1 and PBB-2 were measured at Lawrence Livermore National Laboratory, whereas samples MING, WTASH, MSN, OYT, ATSH, and SWMG were measured at Purdue Rare Isotope Measurement facility (PRIME). N.D.—not determined.

*Isotope ratios were normalized to ^{10}Be standards prepared by Nishiizumi et al. (2007) with a value of 2.85 × 10^{12} and a ^{10}Be half-life of 1.38 × 10^6 yr (Chmeleff et al., 2010).

†^{10}Be/^{9}Be ratios were corrected using a ^{10}Be laboratory blank (n = 2) of 9.15 × 10^{-15} for samples PBB-2, OYT, and MSN, and 9.73 × 10^{-15} for PBB-1, MING, SWMG, ATSH, and WATSH.

§Isotope ratios were normalized to ^{26}Al standards prepared by Nishiizumi et al. (2007) and a ^{26}Al half-life of 0.7 × 10^6 yr.

#^{26}Al/^{27}Al ratios were corrected using a laboratory blank (n = 2) of 4.09 × 10^{-15} for samples PBB-1 and PBB-2, and 0 × 10^{-15} for MING, SWMG, ATSH, WATSH, OYT, and MSN.

**^{27}Al measurements were made using an inductively coupled plasma–atomic emission spectrometer (ICP-AES).

††^{26}Al/^{10}Be ratio and ^{26}Al/^{10}Be age were modeled using Monte Carlo methods described in text. Errors are reported at the (1σ) 68% confidence interval.

§§^{26}Al/^{10}Be age includes a correction for postdepositional production.

on the calculated burial age. In these cases, we constrained the age of abandonment of the terrace overlying the sample using OSL and cosmogenic radionuclide depth-profile dating (Anderson et al., 1996) and corrected for postdepositional production based on the terrace age, its height above the sample, and an assumed instantaneous incision to the current level at the time of terrace abandonment. Furthermore, for samples that were not completely shielded by steep, vertical cliffs, we measured the topographic shielding at the site and the self-shielding (sample thickness, usually 15 cm) for scaling the production rate, except at the Mushi anticline, where these measurements were not collected. Where necessary and possible, we calculated present-day nominal shielding depths when shielding may have been <30 m due to incision and exposure on the incised valley walls. We then calculated the production of each isotope at a constant depth below the surface, including shielding, using Equations 3 and 4, and subtracted this additional ^{26}Al and ^{10}Be concentration from the measured concentrations. See the GSA Data Repository material for more details on the postdepositional production calculations.

The ^{26}Al/^{10}Be ratios and burial ages were calculated following a Monte Carlo approach that included values and 1σ uncertainties for the isotope concentrations, mean half-lives, and terrace ages using simulations of 50,000 trials. We assumed every parameter followed a normal distribution using a mean and standard deviation. All burial age uncertainties are reported at the 68% (1σ) confidence interval.

BURIAL DATING OF GROWTH STRATA: FIELD OBSERVATIONS, SAMPLING, AND RESULTS

In this section, we describe the structural and stratal geometries of the studied faults and folds, followed by details of the sampling at each site. Finally, we discuss the burial age results, correlation to existing magnetostratigraphic sections, and any corrections for postdepositional production that we applied based on our field observations.

Northeast Pamir

Main Pamir Thrust

Observations. The MPT juxtaposes Paleozoic metasediments over Mesozoic and Cenozoic sedimentary rocks. In the field, the MPT is an ~200-m- to ~1-km-thick zone of fractured and brecciated rock, instead of a single fault surface, and it is mapped as several splays (Xinjiang Bureau of Geology and Mineral Resources, 1993). Immediately north of the MPT and south of the Kumtag fault, the Xiyu Formation forms a syncline (Figs. 1 and 4A). On the southern and northern flanks of the syncline, the Xiyu beds dip ~17°N and 12°S, respectively. At the outcrop scale, the Xiyu strata thicken into the core of the syncline.
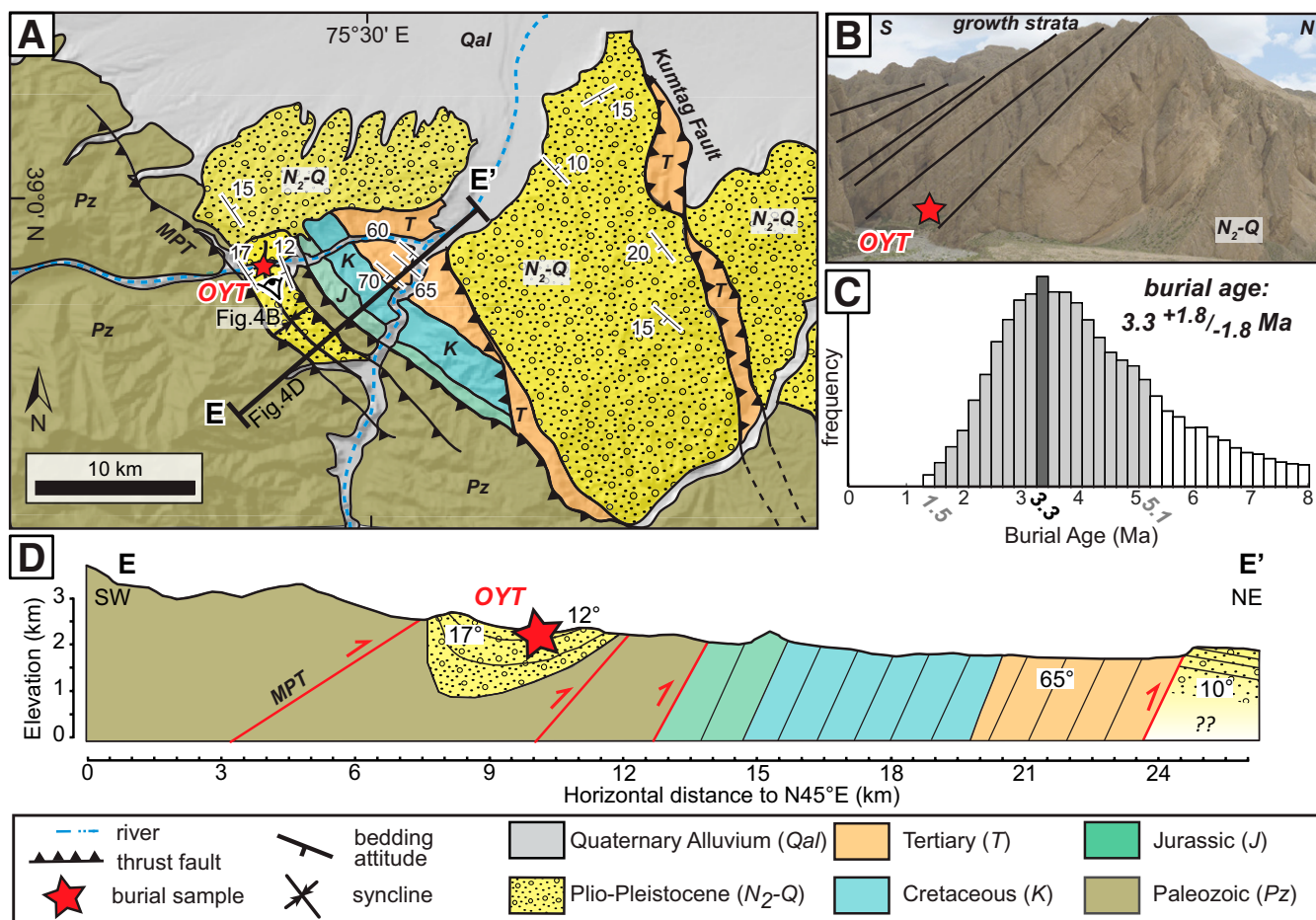
Sampling. We interpret the thickened strata in the syncline as syndepositional growth strata related to deformation on the MPT (Figs. 4B and 4D). We collected a sample (Oytag [OYT]) from the Xiyu Formation in the syncline from a well-shielded cave ~2 m deep within a very narrow slot canyon (~4 m wide, 100+ m tall; Table 1; GSA Data Repository Fig. DR5).

Burial age. Sample OYT had a low a ^{26}Al/^{27}Al ratio that was similar to the ^{26}Al/^{27}Al target blanks (0.1 × 10^{-14} vs. ~0 × 10^{-15}). However, this sample had a low ^{26}Al/^{27}Al ratio uncertainty and a correspondingly low ^{10}Be concentration; thus, we considered the data reliable. The OYT sample from the Xiyu Formation has a simple burial age of 3.3 +1.8/–1.8 Ma (Table 2; Fig. 4C), indicating the MPT was active during the Pliocene or early Quaternary.

Bieertuokuoyi Basin

Observations. The Bieertuokuoyi Basin is a piggyback basin located in the hanging wall of the PFT (Figs. 1 and 5) and immediately north of the Takegai thrust. The stratigraphy of the basin, structural geometries, magnetostratigraphic section, and burial ages were described in detail in Thompson et al. (2015). Here, we summarize the results and present recalculated burial ages using updated production rates, mean lives, and Monte Carlo techniques for ease of comparison with the other ages.

The Takegai thrust places the Miocene Wuqia Group over the Xiyu Formation along a fault that strikes E-W and dips ~30°S. The Xiyu Formation in the footwall of the thrust dips vertically and is locally overturned. To the south, along the Bieertuokuoyi River, the Xiyu Formation also overlies the Miocene Wuqia Group in the hanging wall, separated by an angular unconformity. These strata drape over the tip of the fault, creating growth strata that thicken into the footwall of the thrust (Thompson et al., 2015). At the northern end of the basin, another fault, the PFT dips ~75°SW (Figs. 5A and 5B; Li et al., 2012). The fault places Paleogene gypsum and marine sediments over late Quaternary terrace deposits. Southwest

Figure 4. (A) Simplified geologic map of the Oytag area, near the Main Pamir thrust (MPT). (B) Photo of the growth strata within the Pliocene–Pleistocene Xiyu Formation near Oytag, situated between two splays of the MPT. Red star depicts location of Oytag (OYT) sample. Sample is projected to where it would appear in the section across the valley. (C) Modal and 1σ confidence interval of the burial age. (D) Cross section across the MPT and splays. The burial sample, noted by the red star, was collected in a syncline between the MPT and a fault splay.

of the fault outcrop, a thick (~8 km) sedimentary section spans the entire Cenozoic (Xinjiang Bureau of Geology and Mineral Resources, 1993).

The stratigraphy of the Bieertuokuoyi Basin includes the Xiyu Formation and a finer-grained unit named the "Piggyback Basin" unit (Fig. 5C). At the base of the basin fill, the Xiyu Formation is separated from the Wuqia Group by an erosional unconformity. Within ~500 m of the unconformity, minor angular unconformities, thickening beds, and fanning dips are interpreted as growth strata (Thompson et al., 2015). At the stratigraphic top of the basin, another set of strata can be correlated to growth strata at the southern end of the basin where they overlie the Takegai thrust (Thompson et al., 2015). To date the deposition of the piggyback basin and constrain the ages of growth strata at the top and base, we previously collected a 1.6-km-thick magnetostratigraphic section from the fine-grained Piggyback Basin strata (Fig. 5; Thompson et al., 2015).

Sampling. To help pin the magnetostratigraphic section to the magnetic time scale, we previously collected two burial samples (samples Piggyback Basin 1 and 2 [PBB-1 and PBB-2, respectively]; Table 1; GSA Data Repository Fig. DR2) from the base and top of the section. The sample site (PBB-2) at the top of the section was a smaller cave within a broad opening along tall cliffs of Xiyu Formation. The broader opening was ~46 m tall and ~14 m deep (Table 1; GSA Data Repository Figs.

DR2B and DR2D). The smaller cave we sampled was ~1 m high and ~2 m deep, whereas the cliff face rising above it was >100 m high. Large blocks of Xiyu Formation within the broader opening and at the base of the cliffs indicate ongoing erosion through block collapse. Near the base of the piggyback basin, sample PBB-1 was collected from under an overhang of ~0.5 m within a narrow, deep (~1.5 m wide, 200+ m deep) slot canyon (Table 1; GSA Data Repository Figs. DR2A and DR2C). Despite recent incision, overall shielding remains high at each site.

Burial ages. The two burial cosmogenic ages are 2.9 +1.7/–1.1 and 1.9 +1.4/–1.9 Ma (PBB-1 and PBB-2, respectively) from the bottom and top of the section (Figs. 5C and 5D; Table 2). These ages were used to pin the magnetostratigraphic section to the GPTS. In Thompson et al. (2015), several alternative correlations to the GPTS were proposed and discussed in detail; we summarize the findings here. The preferred correlation, which accounts for the burial ages with their 1σ uncertainties and reasonable sediment-accumulation-rate values and changes, spans from ca. 4.5 to ca. 1 Ma. Two alternative correlations tie the section to ca. 6–2.5 Ma or ca. 6.5–4 Ma. However, these alternative correlations require unreasonable sediment-accumulation-rate values, abrupt rate changes, and the absence of several longer subchrons within these time periods that were missed, despite tightly spaced sample collection. Moreover, the latter alternative correlation falls outside of the 2σ uncertainty of the younger burial sample.
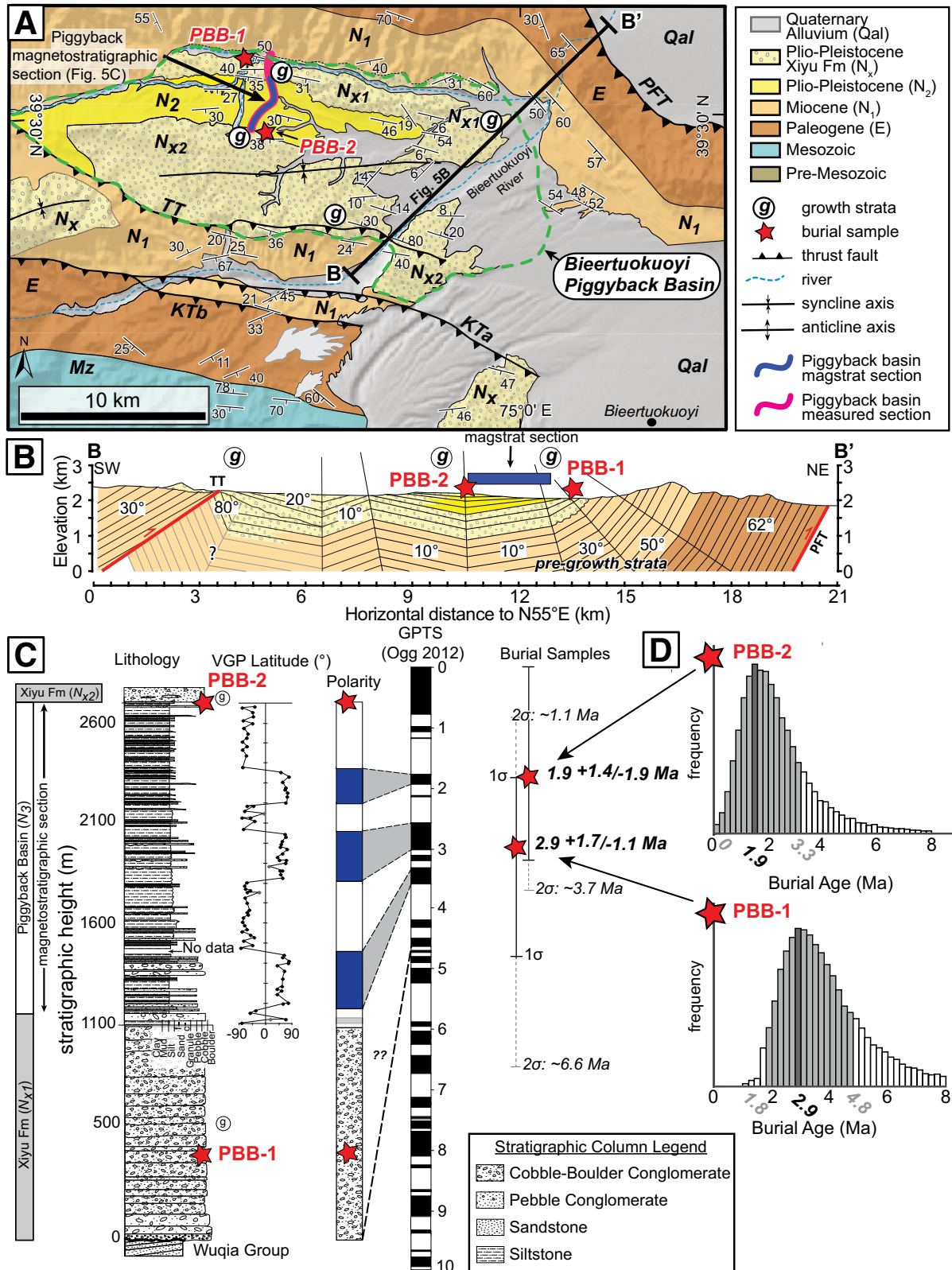
Figure 5. (A) Simplified geologic map of the Bieertuokuoyi Basin. (B) Cross section of the Bieertuokuoyi anticline. (C) Lithology, paleomagnetic data (VGP—virtual geomagnetic pole), resulting magnetic polarity, and correlation to the geomagnetic polarity time scale (GPTS; Ogg, 2012) of the magnetostratigraphic (magstrat) section (Thompson et al., 2015). The red stars mark the location of the cosmogenic burial samples within the section. (D) Modal and 1σ confidence interval of the burial ages. KTa, KTb—strands of the Kenenbierte thrust; PFT—Pamir Frontal thrust; TT—Takegai thrust.

Thus, we prefer to use the correlation that spans from ca. 4.5 to ca. 1 Ma (Fig. 5C). Regardless, any of the correlations support a latest Miocene to early Pleistocene age of the sediments.

In the Bieertuokuoyi piggyback basin, the timing of large-scale collapse of the cliff face that reduced shielding of sample PBB-2 is unknown. Although we assume exposure due to block failure happened very recently (past few thousand years), following persistent incision through the overlying strata, if it had occurred instantaneously at a more distant time in the past, reduced shielding would cause significant postdepositional production. For example, if exposure had occurred ca. 15 ka, the burial age increases by 10% to 2.1 Ma. However, if exposure occurred ca. 100 ka, the burial age increases by almost 80%, to 3.4 Ma. The shape of the sample site (large bowl facing north) and low depth (<6 m) of current nominal shielding of the sample site mean postdepositional nuclide production may have a significant effect (GSA Data Repository Figs. DR2B

and DR2D). However, because we do not know when the shielding was reduced, we use the simple burial age of ~1.9+1.4/–1.9 Ma.

Strata at the top of the section, correlated to growth strata related to the Takegai thrust, date the initiation of the Takegai thrust to ca. 1.9 Ma. Growth strata at the base of the basin date the initiation of the PFT to ca. 6–5 Ma. These data together indicate movement on both the Takegai thrust and PFT during the Pliocene to Quaternary, and they place a constraint on the first deformational episode on the Takegai thrust to at least ca. 2 Ma, and possibly older than 6–5 Ma (Thompson et al., 2015).

Pamir Frontal Thrust

Observations. The PFT, the northernmost fault of the Pamir thrust system, overrides the southwestern limb of the Mingyaole anticline (Figs. 6A and 6B; Li et al., 2012, 2015b). The southwestern limb of the Mingyaole anticline consists of Xiyu Formation dipping ~50° to the south,
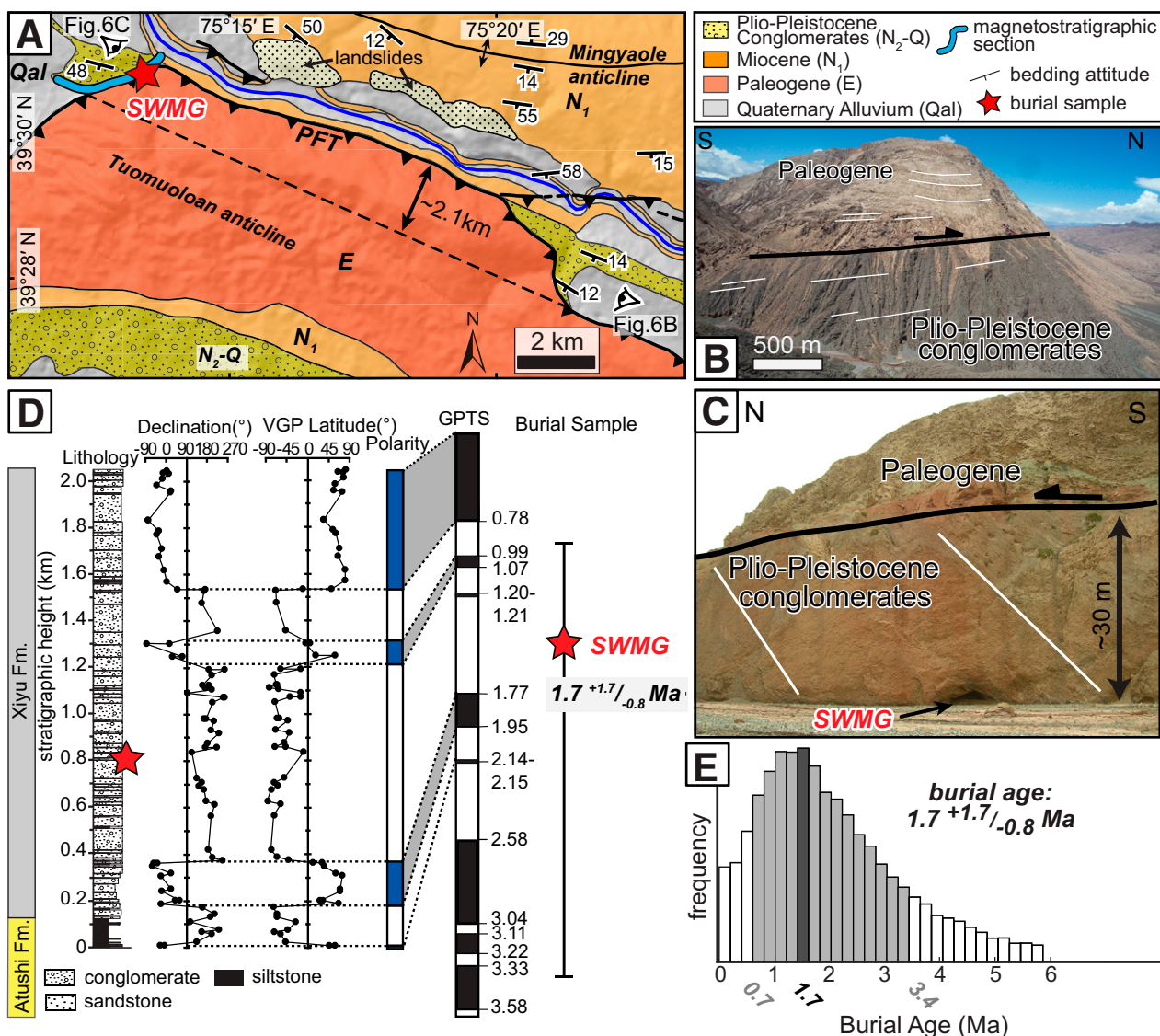

Figure 6. (A) Simplified geologic map of the western end of the Tuomuluoan anticline, Mingyaole anticline, and Pamir Frontal thrust (PFT). (B) Photo of the PFT placing Paleogene marine units over the Pliocene–Pleistocene conglomerates. (C) Photo of the southwest Mingyaole burial sample (SWMG) site, collected from a cave within an incised valley. (D) Magnetostratigraphic data (VGP—virtual geomagnetic pole) and correlation to the geomagnetic polarity time scale (GPTS; Ogg, 2012) for the SW Mingyaole section (Li et al., 2012). Red star indicates burial age and 1σ confidence interval. (E) Modal and 1σ confidence interval of the burial age, including postdepositional production.

but the dip becomes progressively more gentle, to 27°, in overlying strata to the north. Here, the PFT overrides the Xiyu Formation on a nearly horizontal fault plane that dips ~16° to the south, subparallel to the overlying bedding. Field mapping and aerial photo analysis indicate at least 2.2 km of overthrusting (Li et al., 2012). A 1.4-km-thick magnetostratigraphic section through the Xiyu Formation was interpreted to span from ca. 2.15 to 0.35 Ma (Li et al., 2012), based on its correlation to the nearby Mingyaole anticline (Chen et al., 2005).

Sampling. We collected a burial sample from a cave within the Xiyu Formation located within the magnetostratigraphic section (southwest Mingyaole [SWMG]; Table 1). The cave was ~4.5 m deep, and the cliffs above were greater than 30 m high (Fig. 6C; GSA Data Repository Fig. DR7). Incision of the river valley occurred since the Last Glacial Maximum (LGM), based on nearby dated terraces (Li et al., 2012, 2015b; Thompson, 2013; Thompson Jobe et al., 2017), and therefore, we know the sample has been well shielded until recently.

Burial age. The simple burial age is 1.6 +1.8/–0.9 Ma, and the burial age including postdepositional production is 1.7 +1.7/–0.8 Ma (GSA Data Repository Table DR1). Both ages support the previous magnetostratigraphic correlation. Using an age of ca. 0.35 Ma for the top of the section and based on a minimum magnitude of 2.2 km of overthrusting on the PFT (Fig. 6A), the estimated dip-slip rate is >6.4 mm/yr (Li et al., 2012).

Mushi Anticline

Observations. The Mushi anticline is a young, blind-thrust anticline that exposes the Neogene Atushi Formation in its core and Xiyu Formation on its flanks (Fig. 7). On the northern limb of the fold, strata dip steeply north (~68°; Fig. 7). Away from the fold, we observed gentler dips (~26°) and thickening beds. The fold has a total shortening of ~740 m (Li et al., 2013). Deformed Quaternary terraces ranging from ca. 134 to 18 ka, dated using OSL, yielded late Quaternary shortening rates of 1.5 +1.3/–0.5 mm/

yr (Li et al., 2013). The fold's initiation age is estimated to be ca. 0.5 Ma, assuming a constant shortening rate since initiation (Li et al., 2013).

Sampling. We interpreted the thickening beds and gentler dips as growth strata on the northern flank of the fold and collected a burial sample (sample Mushi north [MSN]; Table 1; Fig. 7; GSA Data Repository Fig. DR4) from the strata just below the growth strata. The sample was collected from the bottom of a small overhang at the base of a narrow valley. The cave was shielded by 7 m of Xiyu Formation, and >5 m of upper Quaternary fluvial gravels (GSA Data Repository Fig. DR4). The valley from which the sample was collected was only incised ~30 yr ago, due to the building of a dam downstream that changed the local base level and drove incision of the valley.

Burial age. The simple burial age for sample MSN is 2.0 +2.0/–1.2 Ma (Table 2). Given the relatively shallow depth (≥12 m) since the formation of the fluvial terrace above it, we corrected for postdepositional production. Although we do not have a depositional age for the terrace surface above the burial sample, nearby dated terraces lying above and below this terrace have ages of ca. 55 ka and ca. 15 ka, respectively (Li et al., 2013). Using the ages of dated terraces in the region (Li et al., 2015b, 2013; Thompson, 2013; Thompson Jobe et al., 2017) and the two dated terraces nearby (Li et al., 2013), we estimate this surface dates to ca. 40–30 ka. Including postdepositional production, the MSN burial age indicates that the Mushi anticline began to deform 2.1 +2.1/–1.2 Ma (Table 2; Fig. 7).

Southern Tian Shan

Kelatuo Anticline

Observations. The Kelatuo anticline, the westward continuation of the Atushi anticline, lies at the western end of the Kashi-Atushi fold-and-thrust belt (Figs. 1 and 8A). In the field, the anticline is a south-dipping monocline with the northern limb of the fold cut by the south-vergent
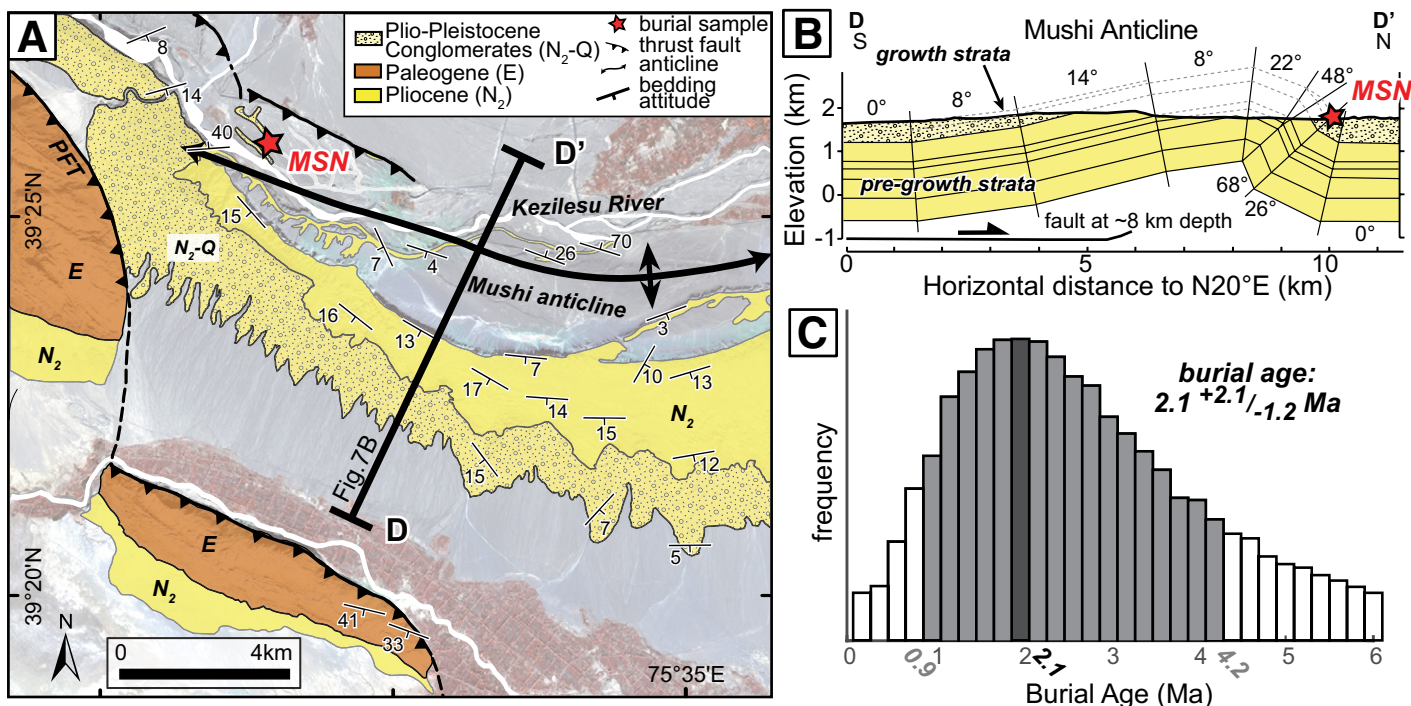

Figure 7. (A) Simplified geologic map of the western end of the Mushi anticline showing location of the Mushi north sample (MSN). PFT—Pamir Frontal thrust. (B) Cross section across the Mushi anticline, illustrating the subsurface structure. (C) Modal and 1σ confidence interval of the burial age, including postdepositional production.
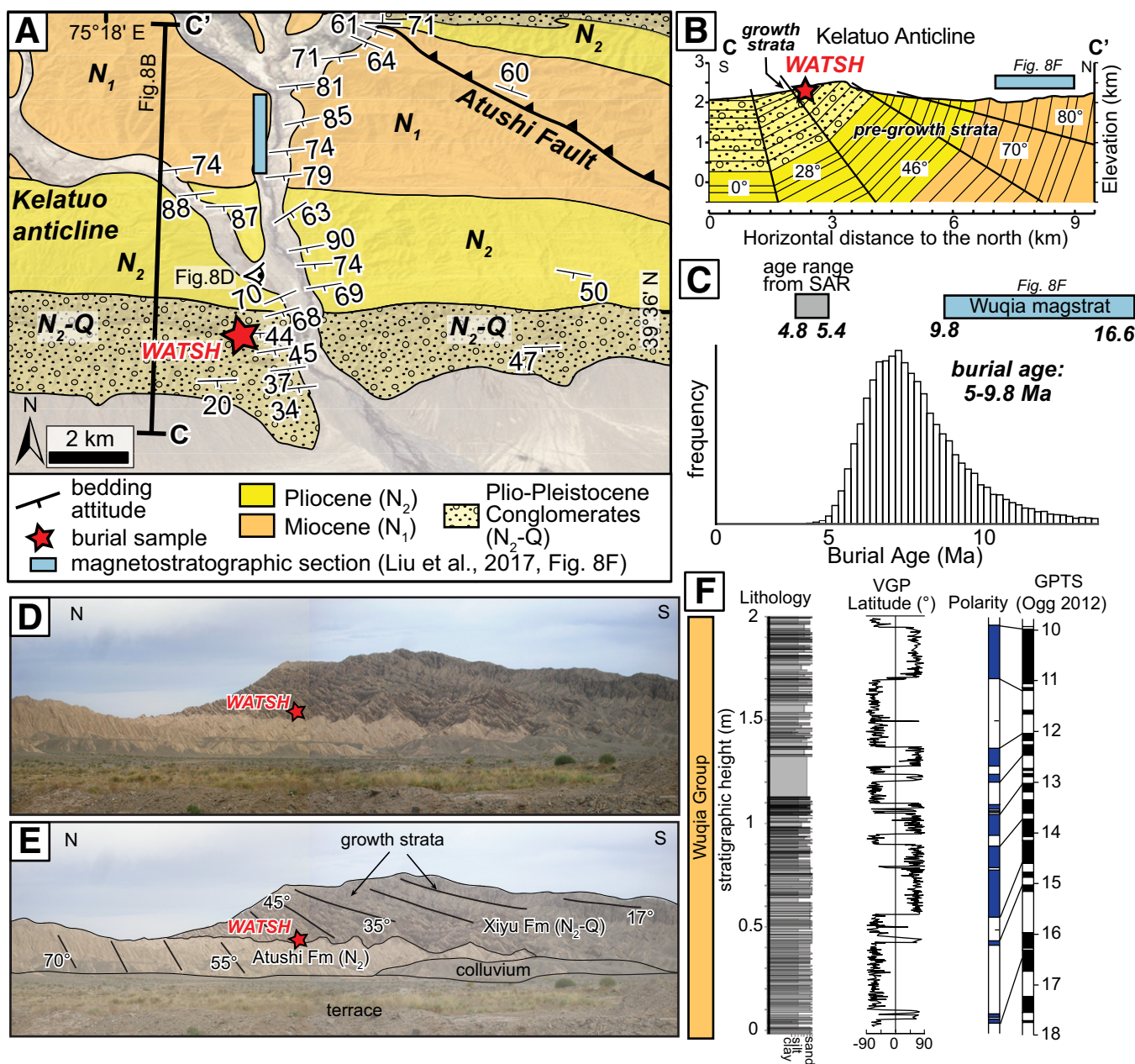
Figure 8. (A) Simplified geologic map of the southern end of the Kelatuo anticline. (B) Cross section across the Kelatuo anticline, illustrating the subsurface structure on its southern limb. (C) Modeled burial age distribution, using ^{26}Al concentrations corresponding to the ^{26}Al/^{27}Al blank ratio of the west Atushi (WATSH) sample. Abbreviation: magstrat—magnetostratigraphic age. (D) Photo of the Neogene Atushi Formation and Pliocene–Pleistocene Xiyu Formation. (E) Photo interpretation on D, showing growth strata on the southern flank of the Kelatuo anticline. (F) Magnetostratigraphic section from Liu et al. (2017) and correlation to the geomagnetic polarity time scale (GPTS; Ogg, 2012). VGP—virtual geomagnetic pole; SAR—sediment-accumulation rate.

Atushi fault (Fig. 8A). This interpretation is consistent with poorly imaged seismic reflection data near the anticline that indicate the structure is cored by Cretaceous strata, with the fold forming above a south-vergent fault (Shang et al., 2004). Structural field data and observations show a progression of gentler dips, thickening beds, and an unconformity near the base of the Xiyu Formation (Liu et al., 2017) on the southern flank of the Kelatuo anticline (Figs. 8A and 8B).

Sampling. We interpreted the strata described above as growth strata, and we collected a burial sample from an overhang within a narrowly incised valley in the Xiyu Formation (sample West Atushi [WATSH];

Table 1; Fig. 8A; GSA Data Repository Fig. DR3). At the sampling site, the bedding dips ~45°S. This sample was collected from bedding ~100 m stratigraphically below the start of the growth strata, which is interpreted to coincide with the change from beds dipping ~45° to beds dipping ~20°. The incised valley is 46 m deep, and the overhang extends 3.3 m from the main channel (GSA Data Repository Fig. DR3). Nonetheless, the channel itself undercuts the cliff such that the overhang extends at least 7 m from the sample site and is ~12 m high (GSA Data Repository Fig. DR3). Field evidence suggests this narrow valley was very recently incised, as indicated by observed collapse of the valley walls, and the presence of a small

debris-flow fan onto a terrace <5 m above the modern river. We estimate the terrace dates to <15 ka, based on dating of terraces in the region (Li et al., 2013, 2015b; Thompson Jobe et al., 2017; Thompson et al., 2018).

Burial age. A high uncertainty on the $^{26}Al/^{27}Al$ ratio (280%), a low $^{26}Al/^{10}Be$ ratio, and a $^{26}Al/^{27}Al$ ratio indistinguishable from our $^{26}Al/^{27}Al$ target blanks within uncertainty (<0.1 × 10^{-14} vs. ~0 × 10^{-15}; Table 2) indicate the sample is likely beyond the reliable range of burial dating. Moreover, the sample had a higher than expected ^{10}Be concentration given the low ^{26}Al concentration, indicating the sample may have been contaminated during preparation, or the initial ratio was not ~6.75.

Additional age constraints come from a magnetostratigraphic section through the Miocene Wuqia Group on the southern flank of the Kelatuo anticline, published by Liu et al. (2017); this section was deposited between 16.6 and 9.8 Ma (Liu et al., 2017). Between the Wuqia Group and the burial sample, ~3.5 km of the Atushi Formation (N$_2$) and Xiyu Formation (N$_2$-Q) are preserved. Using the range of sediment-accumulation rates (200–900 m/m.y.) for the Atushi Formation from the Kashi-Atushi fold-and-thrust belt along strike (Chen et al., 2002; Heermance et al., 2008; Chen et al., 2015), this section corresponds to ~3.9–17.5 m.y. of time

(Fig. 8F). However, given that the average sediment-accumulation rate of the Atushi Formation is at the higher end of the range (between 700 and 800 m/m.y.; Heermance et al., 2008), we contend that the section most likely records ~4.4–5 m.y. of deposition. Thus, the magnetostratigraphic section provides a loose, but independent age constraint, indicating the burial sample should date to between 5.4 and 4.8 Ma (Fig. 8C), at the upper limit of burial dating.

Given the constraints from the magnetostratigraphic section, we know the sample must be younger than ca. 9.8 Ma. To calculate an estimated burial age, we used the low ^{26}Al concentration, which resulted in a burial age of ca. 7.4 Ma, i.e., beyond reliable AMS detection limits and the range of burial dating. Therefore, this sample can only be dated as <9.8 to >5 Ma.

Atushi Anticline and Fault

Observations. The Atushi fault is a south-vergent fault (Figs. 1 and 9) on the southern edge of the Tian Shan that cuts the Atushi anticline (Heermance et al., 2008). The Atushi anticline is cored by the Miocene Wuqia Group, which has been thrust southward on top of overturned Pliocene Atushi Formation. Farther east, growth strata indicate the Atushi anticline
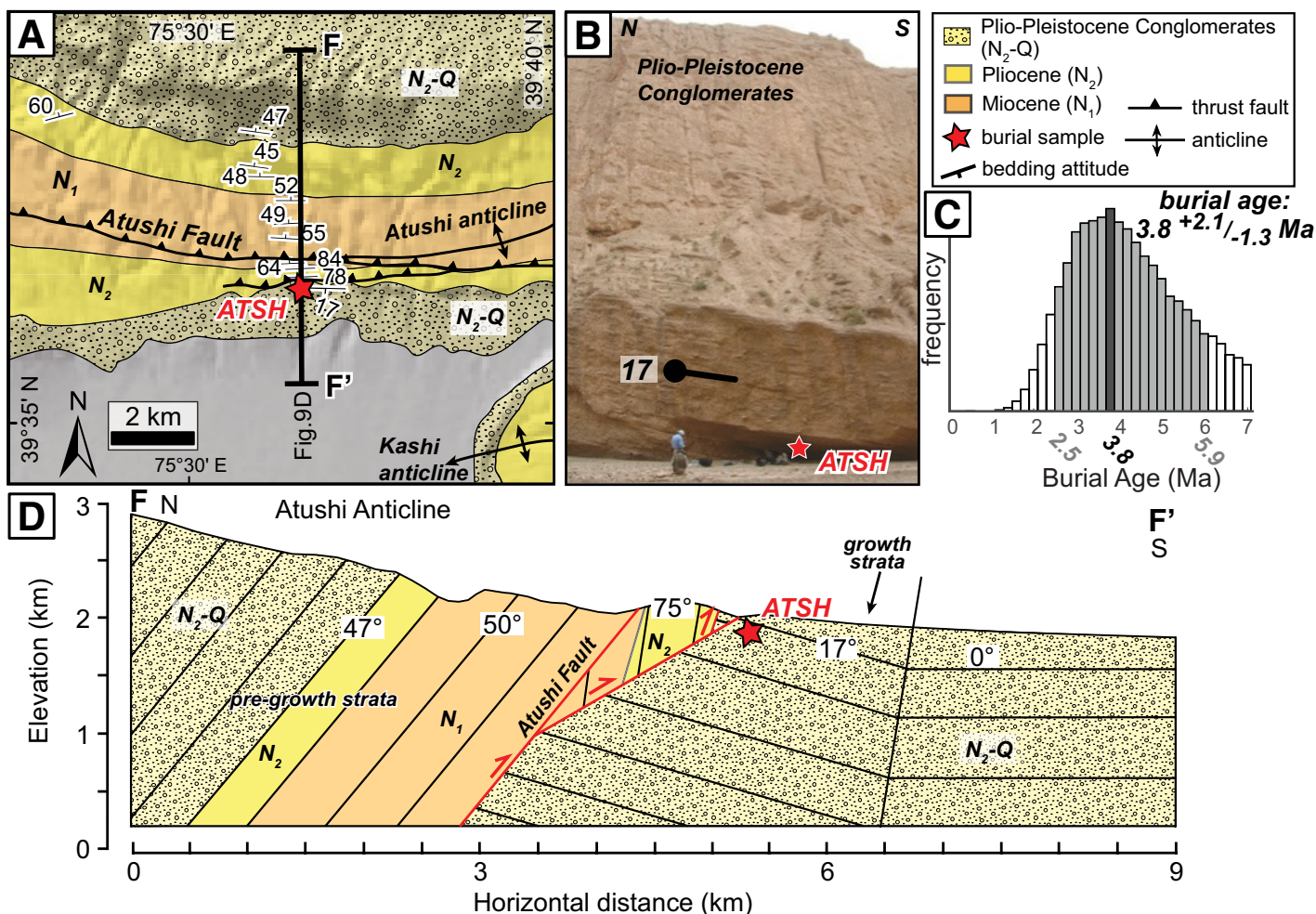

Figure 9. (A) Simplified geologic map of the Atushi anticline and Atushi fault. The Atushi (ATSH) sample was collected from growth strata in the footwall under the Atushi fault. (B) Photo of the sample site, collected from an overhang within an incised valley. Dip symbol shows ~17° dip to south, within growth strata on the southern flank of the Atushi anticline. The splay of the Atushi fault is ~50 m to the left of the photo and projects over the top of the beds from which we sampled. (C) Modal and 1σ interval of the burial age. (D) Cross section across the Atushi anticline and Atushi fault. The burial sample (red star, ATSH) was collected from 17°-southward-dipping beds that are interpreted to be growth strata on the southern limb of the Atushi anticline that have been overridden by the Atushi fault.

initiated ca. 1.4 Ma (Chen et al., 2002; Heermance et al., 2008). On seismic reflection data (line A, Fig. 1B), the fault cuts across the southern limb of the Atushi anticline and dips ~35° to the north (Heermance et al., 2008). In the field, fault splays are visible (Figs. 9A and 9D). The primary fault strikes approximately E-W and dips 33° to the north. Slickenlines from the fault surface have a rake of ~60°, indicating oblique-slip movement. Total shortening on the Atushi fault from seismic reflection data is 10–12 km (Heermance et al., 2008).

Sampling. We collected a burial sample from a cave in an incised valley in beds of the Xiyu Formation dipping ~17°S, from directly underneath a southern splay of the fault on the southern limb of the Atushi anticline (sample Atushi [ATSH]; Table 1; Fig. 9B). We interpret the ~17°S-dipping beds as growth strata on the southern limb of the Atushi anticline, based on our new mapping of the area and mapping from the Kelatuo section ~8 km to the west along strike (Fig. 1). The cave from which we sampled was ~2.3 m deep, and the valley depth was ~64 m (Fig. 9B; GSA Data Repository Fig. DR6). Quaternary incision has reduced the shielding to ~8 m, creating a small strath terrace above the sample site (Fig. 9B).

Burial age. Due to low ^{26}Al concentrations and high ^{26}Al/^{27}Al ratio uncertainties (Table 2), the burial age for this sample also has high uncertainties, yielding a simple burial age of 3.5 +2.1/–1.2 Ma (Table 2; Fig. 9C). Because shielding has been reduced in recent times, but the timing of incision remains unknown, this simple burial age should be considered a minimum age. To estimate postdepositional production, we assumed the small terrace ~8 m above the sample formed ca. 15 ka (Li et al., 2012), resulting in an age of 3.8 +2.1/–1.3 Ma. If the formation of the terrace occurred further into the past, the true burial age would be even older. Thus, we used ca. 3.8 Ma as a minimum age for the deposition of these sediments, indicating deformation initiated ca. 3.8 Ma at this location. Because the strata were deposited and folded prior to being cut by the Atushi fault, this age also implies that the Atushi fault must have initiated after 3.8 Ma, similar to the age estimated from seismic data (Heermance et al., 2008). Using an estimated shortening of 10–12 km (Heermance et al., 2008), the Atushi fault has an average shortening rate of 2.6–3.2 mm/yr since its initiation at this site.

Mingyaole Anticline

Observations. The Mingyaole anticline is a slightly north-vergent detachment fold (Figs. 1 and 10; Scharer et al., 2004, 2006; Li et al., 2015b). Several unconformities are present at the base of the Xiyu Formation (Scharer et al., 2004; Li et al., 2015b), and dips on the southern margin abruptly change (across <100 m horizontally) from 27° to 13° (Fig. 10B). Field observations indicate beds thicken away from the core of the fold (Figs. 10B and 10C). Several late Quaternary terraces span the width of the Mingyaole fold (Scharer et al., 2006; Li et al., 2015a). Near the burial sample site, OSL ages date a gravel fill (1–3 m thick) above a strath terrace surface (T3) lying ~30 m above the incised valley floor (and the burial sample site) to 14.6 ± 2.6 ka (Li et al., 2015b).

Sampling. We interpret the combination of minor angular unconformities, thickening beds, and gentler dips away from the fold core as growth strata (Scharer et al., 2004; Chen et al., 2005). We collected a burial sample beneath an ~3.5-m-deep overhang, with a shielding of ≥10 m (GSA Data Repository Fig. DR1), within an incised valley at the base of the growth strata (Mingyaole [MING]; Table 1) that date to ca. 1.6 Ma (Chen et al., 2005) and that are contained within an already published magnetostratigraphic section that spans from <3.04 and >1.1 Ma.

Burial age. The burial age from the interpreted growth strata is 0.9 +1.1/–0.7 Ma, which includes postdepositional production (Table 2; Figs. 10D and 10E). Postdepositional production had a negligible effect (<1%) due to the high topographic (geometric) and depth shielding of the sample

(GSA Data Repository Fig. DR1). The burial age supports the magneto-stratigraphic correlation of Chen et al. (2005) that indicates the Mingyaole anticline initiated by ca. 1.6 Ma (Fig. 10D).

DISCUSSION

Limitations of Burial Dating of Basin Fill and Growth Strata

In this study of alluvial strata in the western Tarim Basin, we successfully used burial dating, in conjunction with magnetostratigraphic dating, to reliably date coarse-grained basin fill using seven samples with ages spanning from ca. 3.8 Ma to ca. 0.9 (Fig. 11). One sample (WATSH from the Kelatuo anticline) yielded a ^{26}Al/^{27}Al ratio (<0.1 × 10^{-15}) essentially indistinguishable from our ^{26}Al/^{27}Al target blanks (~0 × 10^{-15}; Table 2). Unfortunately, but like many other burial ages (e.g., Kong et al., 2011), the ages we consider reliable have relatively large uncertainties, which primarily resulted from large uncertainties on the Al measurements, as described below.

Similar to any other geochronologic technique, burial dating has limitations based on our assumptions, the geologic setting, and analytical techniques, as follows:

(1) A region with high erosion rates in the source area results in a lower initial concentration of ^{10}Be and ^{26}Al, limiting the maximum age that can be derived, given analytical uncertainties. Nearly all of the samples indicated moderate erosion rates (~100 m/m.y.; Fig. 11), which may have also led to higher uncertainties on the samples. When the initial concentration of the isotopes is low, deposits younger than ca. 5 Ma would have lower concentrations (i.e., OYT), nearing the detection limit of the AMS (~10^4 atoms/g) and resulting in larger uncertainties on younger ages. The ^{10}Be inheritance concentrations from depth profiles on late Quaternary and Holocene fluvial terraces range from 0.68 × 10^4 atoms/g on the northeast Pamir margin to ~30 × 10^4 atoms/g along the southern Tian Shan (Bufe et al., 2017b; Thompson et al., 2018). These inheritance values may be similar to the initial ^{10}Be concentrations in the sediment upon deposition, and they imply that samples from the Pamir margin had lower incoming concentrations than the samples from the Tian Shan, perhaps due to higher Pliocene and Quaternary erosion and exhumation rates in the Pamir (Cao et al., 2013). Importantly, the ^{10}Be concentrations in the burial samples are generally lower than the inheritance values (after correcting for postdepositional production), indicating that, to a first order, the ^{10}Be concentrations in the burial samples are reasonable and realistic.

(2) Erosion from rocks rich in stable Al, Ti, Mg, Fe, or Mn may lead to (i) "dirty" samples, which commonly complicate the ion-exchange column chemistry and subsequent AMS measurements, and (ii) high stable Al concentrations, which result in lower effective ^{26}Al concentrations. Nearly half of our samples had high (20–30 mg) stable Al contents (Table 2), resulting in large uncertainties in the Al AMS measurements and, hence, large uncertainties on the ages (Fig. 11). Other studies have had similar issues when using ^{26}Al in burial dating of basin sediments (Kong et al., 2011; Gunderson et al., 2014; Matmon et al., 2014). Issues, such as "dirty" samples with high concentrations of stable Al, Ti, Mg, or Mn, are difficult to predict a priori before collecting a sample, yet they amplify uncertainties. In addition, low ^{26}Al/^{27}Al ratios and high ^{26}Al/^{27}Al ratio uncertainties (Table 2; GSA Data Repository Table DR2) also contributed to large uncertainties that resulted in uncertainties >100% of the age (e.g., WATSH; Table 2). In our analysis, when Al uncertainties were high, we assumed a 100% uncertainty on the ^{26}Al concentration simply to calculate a permissible age. However, we recognize the actual uncertainties on the age may be larger than reported. In these cases, using burial dating to pin a magnetostratigraphic section may provide an ambiguous
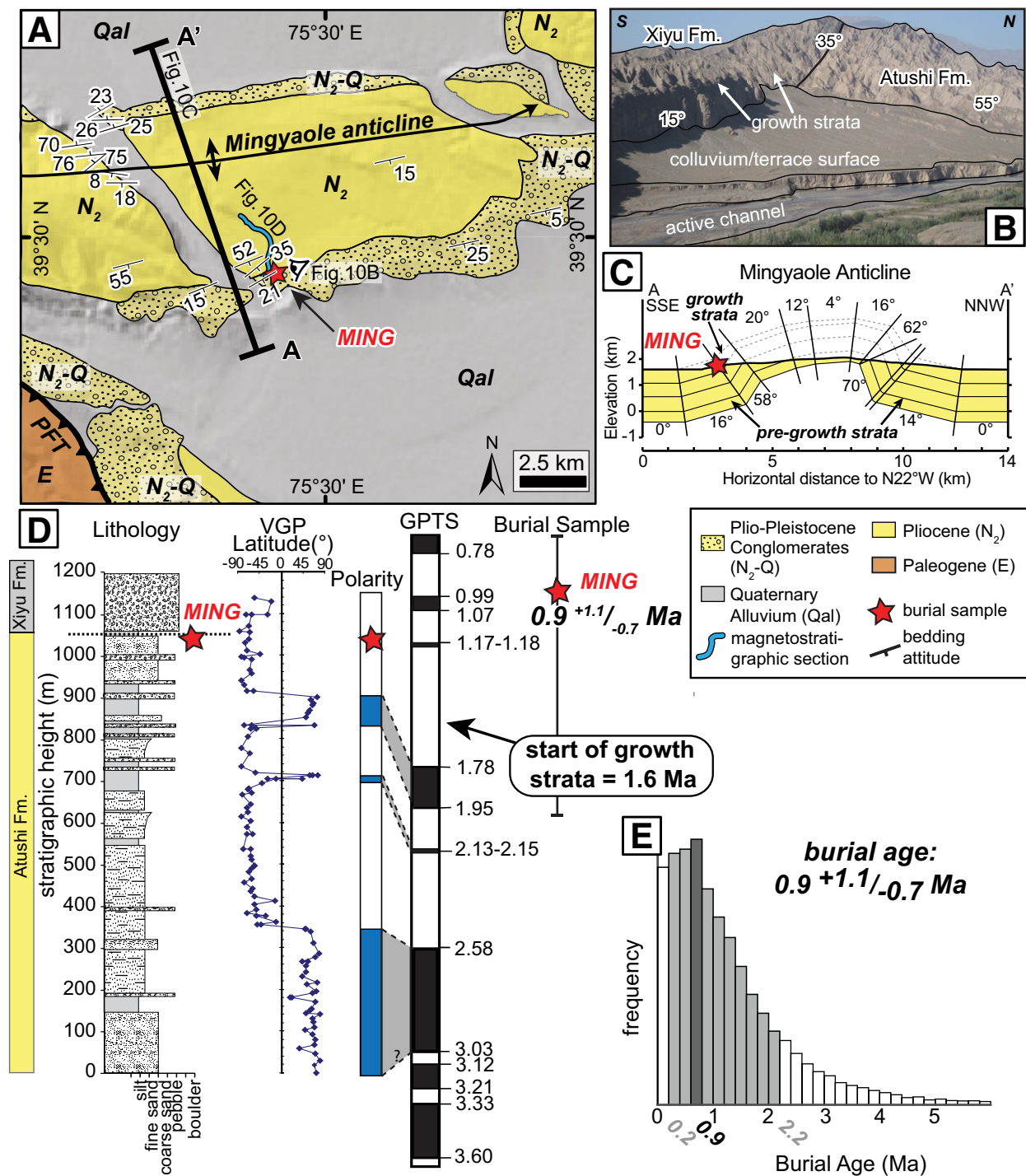
Figure 10. (A) Simplified geologic map of the Mingyaole anticline showing location of the Mingyaole sample (MING). PFT—Pamir Frontal thrust. (B) Field photo and interpretation of structure of the southern limb of the anticline. (C) Cross section of the Mingyaole anticline. (D) Lithology, paleomagnetic data (VGP—virtual geomagnetic pole), resulting magnetic polarity, and correlation to the geomagnetic polarity time scale (GPTS; Ogg, 2012) of the magnetostratigraphic section of the Mingyaole anticline (Chen et al., 2005). The red star marks the location of the cosmogenic burial sample MING within the magnetostratigraphic section. The burial age is shown with 1σ uncertainty. The resulting magnetostratigraphic correlation indicates the growth strata date to ca. 1.6 Ma (Chen et al., 2005). (E) Modal and 1σ confidence interval of the burial age, including postdepositional production.
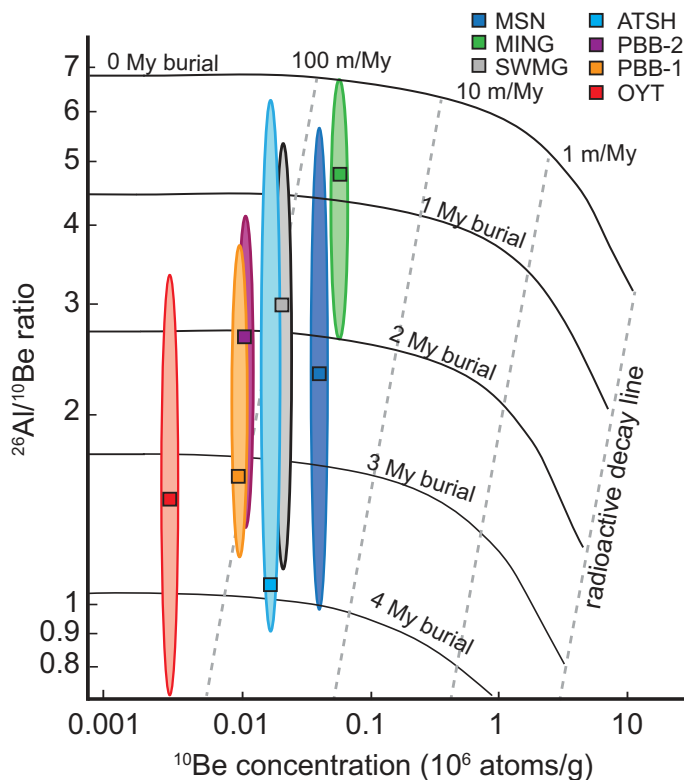
Figure 11. Burial dating plot showing the ^{26}Al/^{10}Be ratio and the ^{10}Be concentration (atoms/g of quartz) in the samples, with 1σ uncertainty envelopes. Radioactive decay of the isotopes (black dashed lines) at different initial source area erosion rates and million-year isochrons for sediment burial following steady erosion are shown. Samples with no burial history will plot along the steady erosion line that intersects the *y*-axis at ~6.75. The different decay rates of the isotopes in buried samples results in the ^{26}Al/^{10}Be ratio plotting below initial production ratio line. The West Atushi (WATSH) sample (5–9.8 Ma) from the Kelatuo anticline is not shown.

correlation, although applying statistical methods, for example, Muzikar and Granger (2006), may increase confidence in a correlation.

(3) A simple burial history is assumed, but issues such as multiple periods of erosion and deposition and postburial nuclide production during incision, exhumation, and/or slow initial sediment burial will change the apparent age of the sample (Matmon et al., 2014; Puchol et al., 2017). Without prior knowledge of the sediment history or application of a third stable nuclide to understand sediment-transport histories of grains (such as ^{21}Ne; Balco and Shuster, 2009; Vermeesch et al., 2010; Matmon et al., 2014), an assumption of a simple burial history is commonly made.

Although we assumed a simple burial history, sediments farther into the foreland may have had significant preburial histories, because the sediment could be sourced not only from the headwaters of the rivers, but also from nearby uplifted Neogene strata. For example, at sites close to the basin margins (Oytag [OYT], Kelatuo anticline [WATSH], Atushi anticline [ATSH]), the sediments were likely eroded from the Paleozoic and Mesozoic units in the hanging walls of the thrusts (Fig. 1). Because of the age of these source sediments, the ^{26}Al and ^{10}Be concentrations were likely very low, having had sufficient time for the isotopes to decay to near zero, and the only measurable concentration results from the most recent period of exhumation and erosion. For structures farther into the foreland, such as Mushi (MSN), Mingyaole (MING), the PFT (SWMG), and the Bieertuokuoyi Basin (PBB-1 and PBB-2), the source areas may have

included recently uplifted Neogene foreland basin strata. In these cases, the incoming initial ^{26}Al/^{10}Be ratio would be lower than the assumed 6.75:1 ratio. This reasoning would imply that the ages from these sites must be interpreted as maximum ages. However, clast counts of the Xiyu strata in the Bieertuokuoyi Basin (Thompson et al., 2015) and field observations of the other sites show that many of the clasts are either granitic or limestone in origin. From these data, we contend that most of the sediment is likely being derived from the exhumed granitic domes and Paleozoic limestone in the nearby mountains, and there may not be a significant contribution from the recently uplifted foreland basin sediments.

Postdepositional production can commonly be ignored if the sample was buried deeply until recent exposure of a sample site, but additional observations and analysis can provide the necessary information needed to calculate additional production and modify ages appropriately. Importantly, in regions with high source-area erosion rates, and hence lower incoming concentrations, the same duration of postdepositional production will have a larger effect on a sample with a lower initial concentration. Therefore, samples in basins that bound rapidly eroding source areas, such as the western Tarim Basin, could be more susceptible to younger apparent ages.

(4) We assumed a density of 2.65 g/cm^3, but uncompacted, recently deposited sediments in a basin or overlying fluvial terraces may have considerably lower densities (e.g., Craddock et al., 2010). Incorrect densities would affect primarily postdepositional production calculations where the sample was not well shielded (>30 m) under primarily younger Quaternary sediments. If a value higher than the true density were used, postdepositional production would be underestimated, resulting in an apparently older age than the true age. If a value lower than the true density were used, additional postdepositional production of the isotopes would increase the isotope concentrations, resulting in an younger apparent age.

(5) The measurement resolution of the AMS places a lower limit on the ratios that can be reliably calculated. Generally, the minimum detection limits are ~10^4 atoms/g (e.g., Matmon et al., 2014). Thus, for samples such as WATSH and OYT, which had concentrations of <1 × 10^4, the resulting uncertainties can be quite high, or an age cannot be reliably calculated (Table 2).

Implications for Regional Deformation

Our new burial ages, combined with previously published magnetostratigraphic sections, provide new dates for the minimum initiation of several structures in the Pamir–Tian Shan convergence zone (Table 3; Figs. 11 and 12). These new data, when integrated with low-temperature thermochronology and magnetostratigraphic data from other studies, illustrate the Neogene–Quaternary propagation of deformation into the western Tarim Basin (Fig. 13).

Northeastern Pamir

On the northeast Pamir margin, deformation appears to have been distributed on several structures simultaneously (Thompson et al., 2015), although deformation likely occurred in three different stages as shortening propagated into the foreland (Fig. 13A). In total, these structures have accommodated ~48.6 km of shortening since the Neogene (Cheng et al., 2016). (1) Deformation initiated on the MPT ca. 25–18 Ma (Sobel and Dumitru, 1997; Bershaw et al., 2012), and continued, perhaps intermittently, until ca. 3.3 Ma (this study). Moreover, the presence of growth strata within an uplifted alluvial fan, possibly of Pleistocene age (?), that sits above an angular unconformity on top of the dated Xiyu Formation (ca. 3.3 ± 1.8 Ma; this study) supports the interpretation that the MPT may have been active during the early Quaternary. Restorations using

TABLE 3. SUMMARY OF SHORTENING, INITIATION OF DEFORMATION, AND LOCAL DEPOSITIONAL AGE OF THE XIYU CONGLOMERATE

| Structure	Shortening (km)	Initiation of deformation (Ma)	Deposition of Xiyu conglomerate (Ma)	Method for age determination	References
Pamir					
Main Pamir thrust	~12	20	$3.3\ ^{+1.8}/_{-1.8}$	Apatite fission track	Sobel and Dumitru (1997); Cheng et al. (2016)
Kenenbierte thrust	~7	Ca. 10?	N.D.	Relative	Thompson et al. (2015); Cheng et al. (2016)
Takegai thrust	~7?	5–6?, 1.9	5–6?, 1.9	magnetostratigraphy, cosmogenic burial age on growth strata	Thompson et al. (2015); Cheng et al. (2016)
Pamir Frontal thrust	~28	5–6	5–6	Magnetostratigraphy, cosmogenic burial age on growth strata	Thompson et al. (2015); Cheng et al. (2016)
Mushi anticline	0.74	$2.1\ ^{+2.1}/_{-1.2}$	$2.1\ ^{+2.1}/_{-1.2}$	Cosmogenic burial age on growth strata	Li et al. (2013); this study
Western Tian Shan					
South Tian Shan fault	>0	20–25	N.D.	Apatite fission track, sedimentation rate increase	Sobel et al. (2006); Chen et al. (2015); Tang et al. (2015)
Kashi Basin thrust	~2–7?	13.6 ± 2.2	N.D.	Apatite fission track	Sobel and Dumitru (1997); Heermance et al. (2008)
Kelatuo anticline	~4–5?	>5	>5	Magnetostratigraphy, cosmogenic burial age from growth strata	Liu et al. (2017); this study
Atushi fault	10–12	>3.8	N.D.	Cosmogenic burial age from crosscutting strata	Heermance et al. (2008); this study
Atushi anticline		Ca. 3.8	$3.8\ ^{+2.1}/_{-1.3}$	Cosmogenic burial age from growth strata	This study
Mingyaole anticline	1.7–3.0	1.6	1.6	Magnetostratigraphy, cosmogenic burial age from growth strata	Chen et al. (2005); this study
Eastern Tian Shan					
South Tian Shan fault	>0	20–25	N.D.	Apatite fission track	Sobel et al. (2006); Heermance et al. (2008)
Muziduke fault	>0	20–25	N.D.	Apatite fission track	Sobel et al. (2006); Heermance et al. (2008)
Kashi Basin thrust	2–7	16.3 ± 0.5	15.5 ± 0.6	Apatite fission track, magnetostratigraphy	Sobel et al. (2006); Heermance et al. (2008)
Tashipishake anticline	4–5	13.1 ± 0.1	N.D.	Magnetostratigraphy	Heermance et al. (2008)
Keketamu anticline	4–5	3.9–4.0	8.6 ± 0.1	Magnetostratigraphy	Heermance et al. (2008)
Atushi anticline	3–4	>1.4	1.9 ± 0.2	Magnetostratigraphy	Chen et al. (2002); Heermance et al. (2008)
Kashi anticline	2–3	1.4 ± 0.3	0.7–1.4	Magnetostratigraphy	Chen et al. (2007); Heermance et al. (2008)

Note: N.D.—not determined.
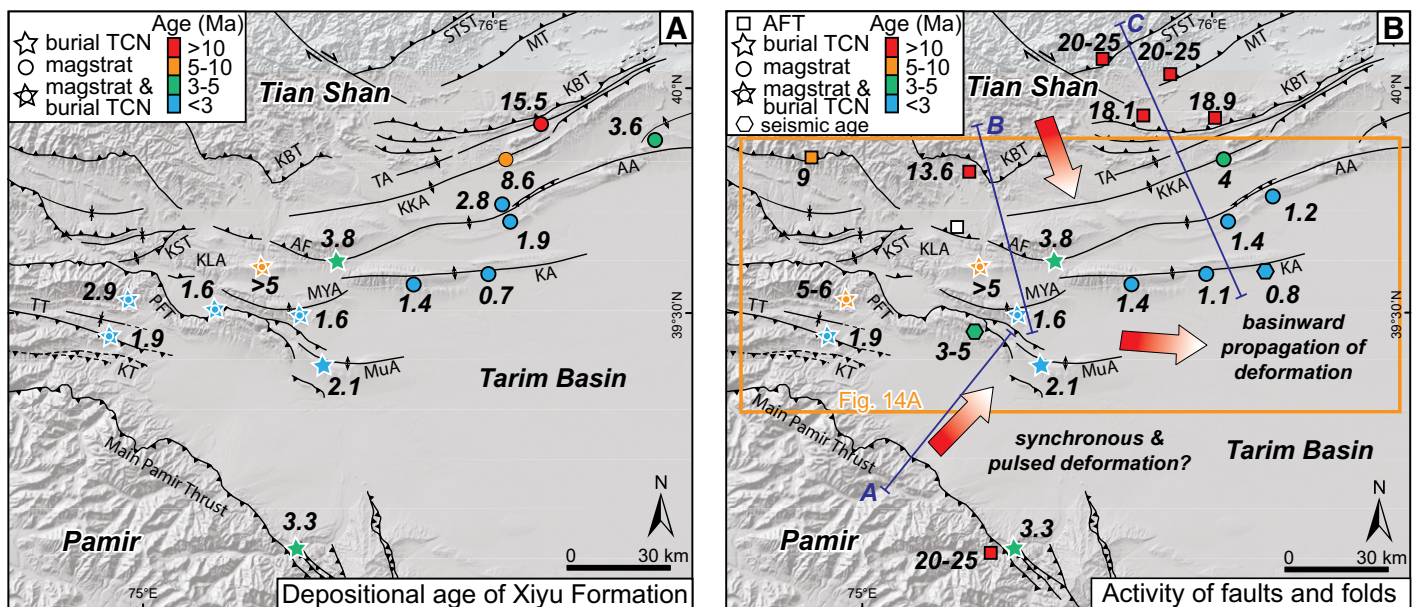
Figure 12. (A) Depositional ages of the Xiyu Formation in the western Tarim Basin, including previous studies; magstrat—magnetostratigraphic, TCN—terrestrial cosmogenic nuclides. (B) Initiation ages of different structures within the western Tarim Basin, illustrating basinward propagation of the orogenic fronts. White square represents unreset apatite fission-track (AFT) ages. Data are from Sobel and Dumitru (1997); Chen et al. (2002, 2005, 2007); Sobel et al. (2006); Heermance et al. (2007); Li et al. (2012); Sobel et al. (2013); Thompson et al. (2015); and Qiao et al. (2016). AA—Atushi anticline; AF—Atushi fault; KA—Kashi anticline; KBT—Kashi Basin thrust; KKA—Keketamu anticline; KLA—Kelatuo anticline; KST—Kangsu South thrust; KT—Kenenbierte thrust; MT—Muzidake thrust; MuA—Mushi anticline; MYA—Mingyaole anticline; PFT—Pamir Frontal thrust; STST—South Tian Shan thrust; TA—Tashipishake anticline; TT—Takegai thrust.
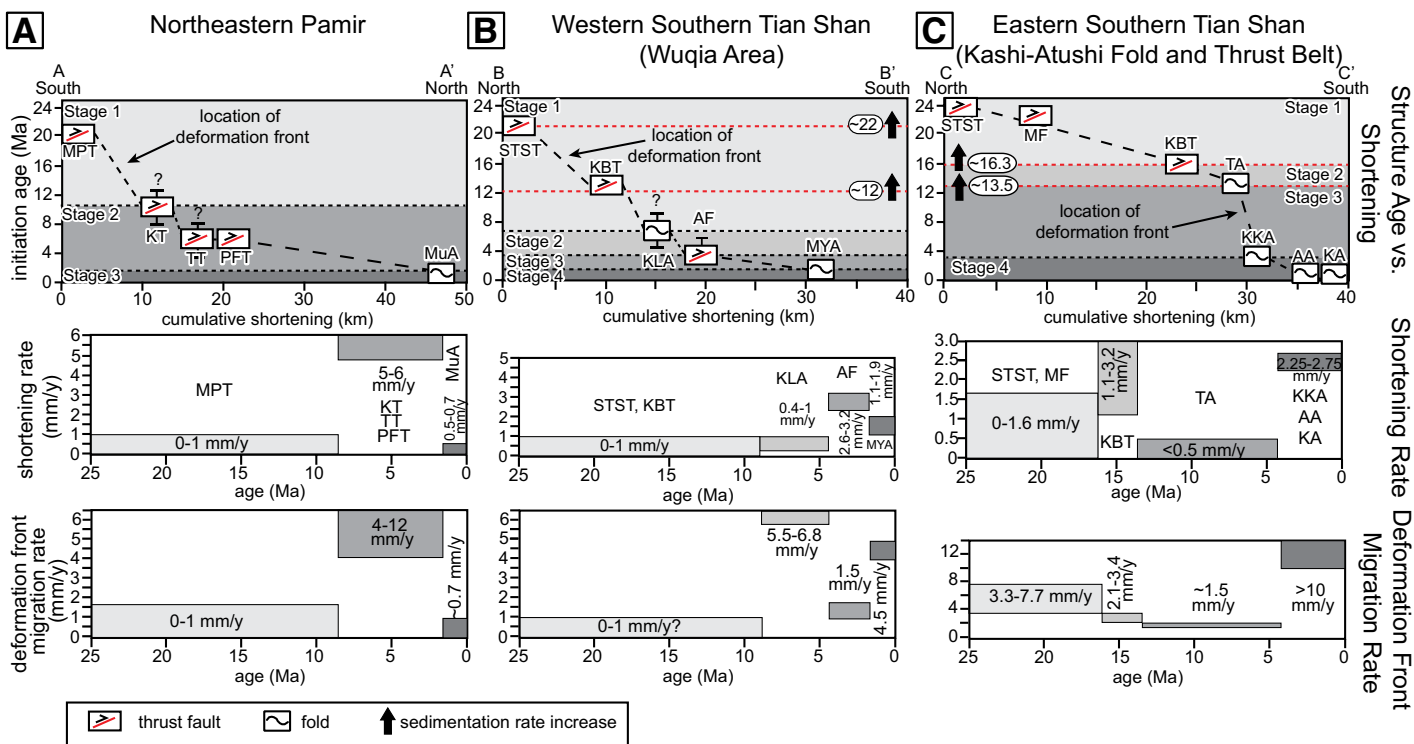
Figure 13. Initiation ages, average shortening rates, and deformation front migration rates for three transects: (A) northeastern Pamir, (B) western southern Tian Shan, and (C) eastern southern Tian Shan. See Figure 12 for location of each transect. Top panel shows the initiation ages (Ma) of different structures from the margin of the orogen toward the foreland. Thrusts and folds are shown in boxes with abbreviated location. Black vertical arrows mark sedimentation rate increases from magnetostratigraphic sections in the basin. Shortening rates assume a total magnitude of shortening from previous studies, described in text, and ages from this and previous studies. Different shades of gray represent different shortening stages, described in text. Bottom panel shows variations in the deformation front migration rate, measured from the closest basin-bounding fault. Data from the eastern Southern Tian Shan are from Heermance et al. (2008). AA—Atushi anticline; AF—Atushi fault; KA—Kashi anticline; KBT—Kashi Basin thrust; KKA—Keketamu anticline; KLA—Kelatuo anticline; KST—Kangsu South thrust; KT—Kenenbierte thrust; MF—Muzidake thrust; MPT—Main Pamir thrust; MuA—Mushi anticline; MYA—Mingyaole anticline; PFT—Pamir Frontal thrust; STST—South Tian Shan thrust; TA—Tashipishake anticline; TT—Takegai thrust.

seismic reflection data (line B, Fig. 1C) suggest at least 12 km of slip on the MPT (Cheng et al., 2016), although these restorations lack supporting field evidence, such as hanging-wall cutoffs. Moreover, unreset apatite fission-track (AFT) and zircon (U-Th)/He ages from the hanging wall of the MPT along strike indicate little exhumation (Sobel et al., 2013). Using the AFT age of 20 Ma as a maximum, a geothermal gradient of 22 °C/km, and estimated fault dip of 30°, the MPT has had an average shortening rate of <1 mm/yr since its initiation. Farther west along the northern margin of the Pamir, in the Alai Valley, the MPT has been active since the Miocene, also with an average rate of <1 mm/yr (Strecker et al., 1995; Coutand et al., 2002), and it remains active today. (2) During the next stage of deformation, several imbricate faults formed ahead of the MPT, leading to a rapid migration of the deformation front at a rate of 4–12 mm/yr (Fig. 13A). The Kenenbierte thrust (Fig. 1) initiated during the middle Miocene (Thompson et al., 2015), followed by the Takegai and Pamir Frontal thrusts in the late Miocene. Furthermore, evidence from the Bieertuokuoyi piggyback basin supports synchronous deformation on the Takegai and Pamir Frontal thrusts between 6–5 and 1.9 Ma (Fig. 5; Thompson et al., 2015; this study), although currently much of the late Quaternary deformation is focused on the PFT (Li et al., 2012; Bufe et al., 2017a; Thompson Jobe et al., 2017). In total, these three faults accommodate most of the shortening along the NE Pamir margin, with the PFT absorbing the largest amount (~28 km; Cheng et al., 2016), resulting in an average shortening rate of 5–6 mm/yr. (3) The final stage

of Pamir deformation is marked by the initiation of the Mushi anticline ca. 2.1 Ma, as constrained by the cosmogenic burial age in our study. In this phase, the deformation front migrated at a slower rate of ~0.7 mm/yr, possibly slowed by impingement of the southward-propagating Tian Shan deformation. Furthermore, the average shortening rate since initiation on the Mushi anticline is 0.5–0.7 mm/yr, which is much slower than the folds on the southern Tian Shan, perhaps because the PFT remains the most active structure on the NE Pamir margin (Thompson Jobe et al., 2017).

Western Southern Tian Shan

On the southern margin of the Tian Shan, deformation is clearly younger southward into the foreland (Fig. 12B; Heermance et al., 2008). On the western southern Tian Shan, deformation stepped basinward in four primary phases (Fig. 13B). The first stage is marked by the initiation of the South Tian Shan fault and Kashi Basin thrust (Fig. 1). The South Tian Shan fault, which initiated ca. 20 Ma (Sobel et al., 2006), accommodates an unknown amount of shortening, but at least 3.5 km of exhumation (Sobel et al., 2006; Heermance et al., 2008). Older detrital AFT (25–13 Ma) samples in Miocene-age strata north of Wenguri (Sobel and Dumitru, 1997) and ca. 16–18 Ma AFT ages from Cretaceous strata near Ulugqat (Yang et al., 2014) support the interpretation of earlier thrusting closer to the margin of the southern Tian Shan. In addition, an increase in sediment-accumulation rates ca. 22 Ma from Miocene strata in the Tierekesazi and Baxubulak magnetostratigraphic sections

supports this timing (locations in Fig. 1; Chen et al., 2015; Tang et al., 2015). Moreover, samples from the westward continuation of the Kashi Basin thrust near the Kuzigongsu River yielded AFT cooling ages of 13.6 ± 2.2 Ma (Figs. 1 and 12), suggesting rapid exhumation and shortening (Sobel and Dumitru, 1997). This age is supported by an increase in the sediment-accumulation rate of middle Miocene sediments ca. 12 Ma in a section ~20 km to the west (location in Fig. 1; Chen et al., 2015), and it may have continued or was followed by another pulse ca. 6–7 Ma, based on sediment-accumulation rates from Neogene sedimentary rocks near Ulugqat (Qiao et al., 2017) and Mutule (Qiao et al., 2016), although these magnetostratigraphic sections lack absolute age control to the GPTS. We estimate a total shortening of ~2–7 km along the Kashi Basin thrust, relying on estimates from seismic lines ~10 km to the east (line A, Fig. 1B; Heermance et al., 2008). These estimates result in an average shortening rate of 0–1 mm/yr and a deformation-migration rate of <1 mm/yr. The second stage is marked by the growth of the Kelatuo anticline, which initiated >5 Ma (this study), as deformation propagated toward the basin at a rate of 5.5–6.8 mm/yr. Because we do not know the total shortening accommodated by the Kelatuo anticline, we assume it has a similar magnitude of shortening to folds farther east that involve similar stratigraphy. We use an estimated shortening of ~4–5 km, based on shortening calculated from the Keketamu anticline and other anticlines in the Kashi-Atushi fold-and-thrust belt (Heermance et al., 2008), resulting in an average shortening rate of ~0.4–1 mm/yr. The third stage is the initiation of the Atushi fault, which we constrain in this study at ca. 3.8 Ma, when the deformation front remained near the same position, but may have migrated southward at a rate of ~1.5 mm/yr. Based on seismic interpretations <10 km east of burial sample ATSH (line A, Fig. 1B), the Atushi fault accommodated 10–12 km of shortening (Heermance et al., 2008), resulting in an average shortening rate of 2.6–3.2 mm/yr. The final stage of migration of the deformation front is the initiation of the Mingyaole anticline ca. 1.6 Ma, which accommodated 1.7–3 km of shortening at an average shortening rate of 1.1–1.9 mm/yr (Chen et al., 2005; this study).

Eastern Southern Tian Shan

Farther east, Heermance et al. (2008) also documented four stages of deformation into the foreland using magnetostratigraphy (Fig. 13C). Stage 1 is marked by initiation of the South Tian Shan thrust and Muziduke fault (Fig. 1) at 20–25 Ma (Sobel et al., 2006), which propagated southward into the basin at rates between 3.3 and 7.7 mm/yr. During stage 2, the initiation of the Kashi Basin thrust began at ca. 16.3 ± 0.5 Ma as the deformation front moved southward at a rate of 2.1–3.4 mm/yr (Heermance et al., 2008). The initiation of the Tashipishake anticline at 13.1 ± 0.1 Ma marks stage 3, with a decrease in southward propagation to ~1.5 mm/yr, whereas during the fourth stage, rapid southward propagation of deformation, at rates of >10 mm/yr, formed the Keketamu, Atushi, and Kashi anticlines beginning ca. 4.0–3.9 Ma (Heermance et al., 2008).

Patterns of Lateral Deformation Propagation

We observed a west-to-east younging of ages on folds within the Pamir–Tian Shan forelands (Fig. 12), as well as an eastward lateral propagation of individual folds. Older ages and both higher structural and greater topographic relief (Scharer et al., 2004; Heermance et al., 2008) on folds farther west in the foreland indicate deformation began earlier in the west, and, as the Pamir and Tian Shan progressively converged, deformation propagated eastward. Such lateral propagation could be expected during oblique closure between these nonparallel mountain fronts, where the western ends of the faults and folds are already pinned, inhibiting westward propagation of deformation (e.g., Dorr et al., 1977).

Most of the Neogene–Quaternary folds display eastward lateral propagation (Fig. 14), evident in the topography, total shortening variations across the folds, structural relief, and ages of growth strata measured laterally along the folds (Scharer et al., 2004; Chen et al., 2007; Heermance et al., 2008; Li et al., 2013, 2015b). Our new burial ages for the Kelatuo anticline (>5 Ma, 0 km) and for the western Atushi anticline (ca. 3.8 Ma, 20 km), combined with ages on growth strata farther east along the Atushi anticline of ~1.4 Ma (70 km) and 1.2 Ma (80 km), indicate the fold may have propagated eastward during the Pliocene to Quaternary (Chen et al., 2002; Scharer et al., 2004; Heermance et al., 2008) at unsteady rates from 15 to 50 km/m.y. (Fig. 14B). Previous work on the Kashi anticline found a similar eastward propagation at unsteady rates from 15 to 115 km/m.y. using growth strata dating from 1.4 to 0.8 Ma (Fig. 14C; Chen et al., 2007; Heermance et al., 2008). However, we caution that the ages at the Kelatuo and Atushi anticlines may be maximum ages because we do not know their preburial cosmogenic history.

On the northeast Pamir margin, the PFT appears older at its western end, with a late Miocene initiation age (Thompson et al., 2015). Approximately 40 km toward the east at the western end of the Mushi and Aismaola anticlines, seismic reflection data (line B, Fig. 1C) indicate the unconformity at the base of the Xiyu Formation changes character (Cheng et al., 2016) as it becomes more flat-lying and shallower, and the overall topography decreases eastward into the western Tarim Basin. Moreover, the Xiyu Formation merges with the modern alluvial piedmont at the eastern end of the PFT and constitutes the present-day piggyback basin, suggesting it has a younger age than the older, deformed and incised piggyback basin to the west (Thompson et al., 2015). Alternatively, the apparently younger age of the PFT to the east may be due to increased erosion that led to beveling of topography and the change in strike of the fault from approximately east-west to northwest-southeast at its far eastern end (Figs. 12 and 14A). The Mushi anticline emerges topographically where the surface expression of the PFT ends, indicating deformation may be transferred onto the younger Mushi fold farther east in the foreland (Fig. 14D). The Mushi anticline initiated 2.1 +2.1/–1.2 Ma. Topography, structural relief, and eastward-tilted fluvial terraces support eastward propagation of the Mushi anticline until ca. 134 ka, when the tip became pinned, and the fold began to grow primarily via lateral rotation (Li et al., 2013).

Unsteady Basinward Deformation Propagation

Together, these data indicate deformation is propagating southward from the Tian Shan, northward from the Pamir into the foreland, and eastward into the Tarim Basin, as the impinging orogens zipper the intervening Tarim Basin closed. Moreover, the available data also indicate: (1) deformation along the NE Pamir margin did not step unidirectionally outward, but it instead displays perhaps alternating and synchronous deformation on the Main Pamir, Takegai, and Pamir Frontal thrusts (Fig. 12), and (2) the hinterland currently deforms at modest deformation rates, indicating the majority of deformation has been accommodated along the frontal structures of both orogens since ca. 1 Ma (Bufe et al., 2017b; Thompson Jobe et al., 2017).

These data support models that suggest out-of-sequence thrusting and hinterland deformation are required to maintain a critically tapered wedge on the margins of growing orogens experiencing hinterland denudation (Davis et al., 1983; Dahlen et al., 1984; Dahlen, 1990). Numerical (Naylor and Sinclair, 2007) and sandbox (Gutscher et al., 1996) modeling indicates that the outward propagation of thrust-related deformation is cyclical, and it alternates between periods of outward thrusting and internal thickening. The activity of any given thrust fault in the system is then dictated by the convergence-parallel length of the thrust sheet, i.e., the displacement
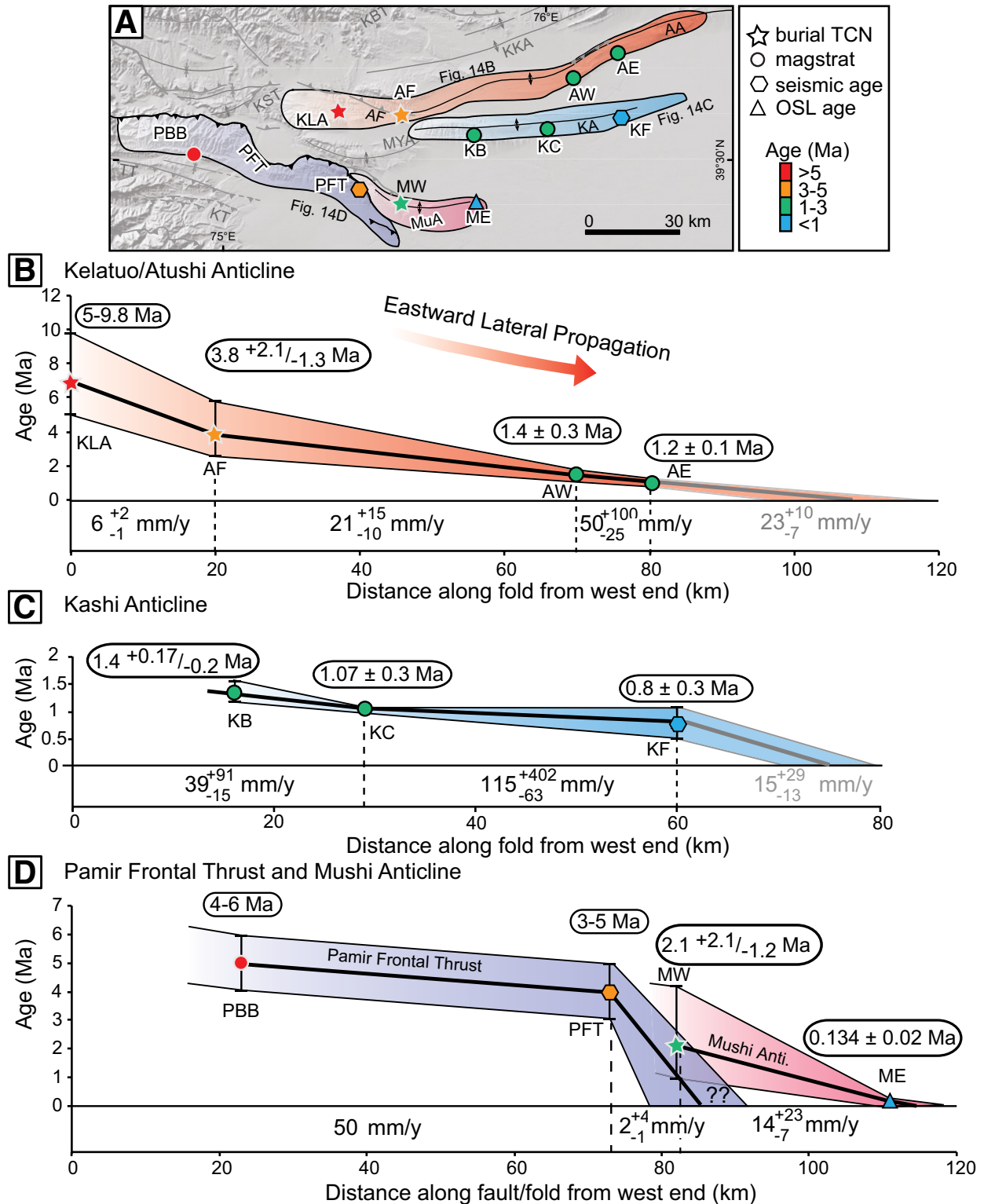
Figure 14. (A) Simplified structural map of the Pamir–Tian Shan convergence zone, showing locations of dated sites and ages of growth strata and distance along fold (from the west) for the (B) Kelatuo/Atushi anticline, (C) Kashi anticline, and (D) Pamir Frontal thrust and Mushi anticline. Gray lines and lighter coloring on eastern ends of Atushi and Kashi folds indicate speculative propagation based on the lack of surface expression of deformation. Abbreviations: magstrat—magnetostratigraphic; TCN—terrestrial cosmogenic nuclides; OSL—optically stimulated luminescence. Data are from this study, Chen et al. (2002, 2007), Heermance et al. (2008), Li et al. (2013), Thompson et al. (2015), and Cheng et al. (2016). Structures: AA—Atushi anticline; AF—Atushi fault; KST—Kangsu South thrust; KA—Kashi anticline; KBT—Kashi Basin thrust; KKA—Keketamu anticline; KT—Kenenbierte thrust; MYA—Mingyaole anticline; MuA—Mushi anticline; PFT—Pamir Frontal thrust; TT—Takegai thrust. Sites: AE—Atushi east; AF—Atushi fault; AW—middle Atushi; KB—Kashi Town; KC—Kashi central; KF—Kashi far; KLA—Kelatuo anticline; MW—Mushi west; ME—Mushi east; PBB—Bieertuokuoyi piggyback basin.

length along the thrust sheet (as controlled by the thickness of the basin fill, the internal strength of the foreland basin sediments, and the friction on the basal detachment; Platt, 1988), divided by the regional convergence rate (Naylor and Sinclair, 2007). On the northeastern Pamir, which has a structural style dominated by thrust faults, the lengths of the thrust sheets are ~12 to ~30 km. Using a regional convergence rate of ~6–9 mm/yr (Zubovich et al., 2016), we estimate the time scale of internal variability (i.e., the inherent tectonic variability of a thrust wedge; Naylor and Sinclair, 2007) of thrusting is ~1.3–5 m.y. The timing of forward propagation of thrust faults and fault-related folds in the foreland approximately match these time scales (Figs. 12 and 13).

However, these models may vary for forelands with variable structural styles, such as the Tian Shan foreland, where the structural style changes from steep thrust faults on the margins to detachment folds in the foreland (Heermance et al., 2008). We speculate that the difference in the deformation propagation timing and rates between the hinterland thrusts and the folds in the foreland is related to the stratigraphic units involved and the structural styles, in addition to the inherent tectonic variability factors discussed above. The transition from steeply dipping basement thrusts within strong Paleozoic and Mesozoic rock units to fault-related folds and more gentle thrusts (i.e., PFT) in the weaker foreland sediments leads to a more rapid propagation of the deformation front (Heermance et al., 2008; Wang et al., 2016).

Time-Transgressive Xiyu Formation

Although not the focus of our targeted sampling, our new burial ages also date the Miocene–Pleistocene Xiyu Formation around the margins of the western Tarim Basin (Fig. 12A; Table 3); these dates highlight the diachronous deposition of the Xiyu Formation within the western Tarim Basin (Heermance et al., 2007; Charreau et al., 2009; Qiao et al., 2016). Ages of the Xiyu conglomerate range from >5 to <1 Ma based on burial ages from this study, but across the southern Tian Shan foreland, initial Xiyu deposition ranges from ca. 15 Ma in northerly outcrops to <1 Ma in the southern part of the foreland (Chen et al., 2002, 2007; Heermance et al., 2007; Qiao et al., 2016), where it merges with the modern alluvial piedmont. The deposition of the Xiyu conglomerate was apparently continuous and prograded south over time in the Tian Shan.

Similar ages of initial local deposition of the Xiyu conglomerates have been documented on the NE Pamir margin, with ages ranging from ca. 5–6 Ma to <1 Ma (Li et al., 2012; Thompson et al., 2015; this study) at the Pamir–Tian Shan interface, but ages are as old as ca. 14 Ma at Aertashi, along strike to the south (Blayney et al., 2016). As in the southern Tian Shan, a similar depositional history emerges in the northeast Pamir, with the Xiyu conglomerate prograding northward since ca. 14 Ma to the present. However, in contrast to the southern Tian Shan, large (3+ km) sections of finer-grained facies occur within the Xiyu Formation in the NE Pamir, indicating pulsed progradation and retraction of the gravel front (Thompson et al., 2015) or a diversion of major rivers resulting from uplift on the PFT. Moreover, Xiyu deposition appears to have occurred repeatedly in the same position in the foreland (e.g., the Bieertuokuoyi piggyback basin), possibly due to changing climatic conditions or to synchronous and/or pulsed movement on faults along the NE Pamir margin (Thompson et al., 2015).

CONCLUSIONS

Dating coarse-grained growth strata on the flanks of folds remains a challenge in areas with few volcanic units and sparse biostratigraphy. Burial dating has emerged as a unique way to date such strata in late Cenozoic basins. We present eight new $^{26}Al/^{10}Be$ cosmogenic burial ages

from Pliocene–Pleistocene sediments from the western Tarim Basin in NW China. Using these ages, we demonstrate an innovative use of burial dating to place multiple age constraints on depositional sequences and to define the initiation of activity on individual structures, especially large-scale folds, on the margins of growing orogens. These samples were strategically collected from within or just beneath growth strata and from sedimentary units in the footwalls of young faults, thereby placing maximum ages on the initiation of deformation of individual structures within the basin.

Burial ages are most reliable when they derive from slowly eroding source terranes, have been deeply and rapidly buried, and have only been exhumed very recently. Placing constraints on any of the commonly unknown variables, such as the rate of sediment burial, time in transport in the fluvial system, or the timing of recent incision and postdepositional exposure, helps to limit the uncertainties associated with burial ages. Where feasible, we combined our burial ages with magnetostratigraphic sections to place further constraints on the deposition of the sediments in the basins and the deformation of nearby structures.

Our results document the late Neogene and Quaternary growth of both the Pamir and Tian Shan orogens, showing both eastward propagation of deformation at rates up to 115 km/m.y., and basinward growth of both orogens since the Miocene at rates up to 12 km/m.y. as they zippered closed the western Tarim Basin.

REFERENCES CITED

Amidon, W.H., and Hynek, S.A., 2010, Exhumational history of the north central Pamir: Tectonics, v. 29, TC5017, https://doi.org/10.1029/2009TC002589.

Anderson, R.S., Repka, J.L., and Dick, G.S., 1996, Explicit treatment of inheritance in dating depositional surfaces using in situ ^{10}Be and ^{26}Al: Geology, v. 24, p. 47–51, https://doi.org/10.1130/0091-7613(1996)024<0047:ETOIID>2.3.CO;2.

Balco, G., and Rovey, C.W., 2010, Absolute chronology for major Pleistocene advances of the Laurentide ice sheet: Geology, v. 38, p. 795–798, https://doi.org/10.1130/G30946.1.

Balco, G., and Shuster, D.L., 2009, $^{26}Al-^{10}Be-^{21}Ne$ burial dating: Earth and Planetary Science Letters, v. 286, p. 570–575, https://doi.org/10.1016/j.epsl.2009.07.025.

Balco, G., Stone, J.O., Lifton, N.A., and Dunai, T.J., 2008, A complete and easily accessible means of calculating surface exposure ages or erosion rates from ^{10}Be and ^{26}Al measurements: Quaternary Geochronology, v. 3, p. 174–195, https://doi.org/10.1016/j.quageo.2007.12.001.

Balco, G., Soreghan, G.S., Sweet, D.E., Marra, K.R., and Bierman, P.R., 2013, Cosmogenic-nuclide burial ages for Pleistocene sedimentary fill in Unaweep Canyon, Colorado, USA: Quaternary Geochronology, v. 18, p. 149–157, https://doi.org/10.1016/j.quageo.2013.02.002.

Bally, A.W., Ming Chou, I., Clayton, R., Heugster, H.P., Kidwell, S., Meckel, L.D., Ryder, R.T., Watts, A.B., and Wilson, A.A., 1986, Notes on sedimentary basins in China, Report of the American Sedimentary Basins Delegate to the People's Republic of China, August 17–September 8, 1985: U.S. Geological Survey Open File Report 86-327, 108 p.

Beamud, E., Muñoz, J.A., Fitzgerald, P.G., Baldwin, S.L., Garcés, M., Cabrera, L., and Metcalf, J.R., 2011, Magnetostratigraphy and detrital apatite fission track thermochronology in syntectonic conglomerates: Constraints on the exhumation of the South-Central Pyrenees: Basin Research, v. 23, p. 309–331, https://doi.org/10.1111/j.1365-2117.2010.00492.x.

Bershaw, J., Garzione, C.N., Schoenbohm, L., Gehrels, G., and Tao, L., 2012, Cenozoic evolution of the Pamir plateau based on stratigraphy, zircon provenance, and stable isotopes of foreland basin sediments at Oytag (Wuyitake) in the Tarim Basin (west China): Journal of Asian Earth Sciences, v. 44, p. 136–148, https://doi.org/10.1016/j.jseaes.2011.04.020.

Blayney, T., Najman, Y., Dupont-Nivet, G., Carter, A., Millar, I., Garzanti, E., Sobel, E.R., Rittner, M., Andò, S., Guo, Z., and Vezzoli, G., 2016, Indentation of the Pamirs with respect to the northern margin of Tibet: Constraints from the Tarim Basin sedimentary record: Tectonics, v. 35, p. 2345–2369, https://doi.org/10.1002/2016TC004222.

Bookhagen, B., and Strecker, M.R., 2012, Spatiotemporal trends in erosion rates across a pronounced rainfall gradient: Examples from the southern Central Andes: Earth and Planetary Science Letters, v. 327–328, p. 97–110, https://doi.org/10.1016/j.epsl.2012.02.005.

Bufe, A., Bekaert, D.P.S., Hussain, E., Bookhagen, B., Burbank, D.W., Thompson Jobe, J.A., Chen, J., Li, T., Liu, L., and Gan, W., 2017a, Temporal changes in rock-uplift rates of folds

in the foreland of the Tian Shan and the Pamir from geodetic and geologic data: Geophysical Research Letters, v. 44, p. 10,977–10,987, https://doi.org/10.1002/2017GL073627.

Bufe, A., Burbank, D.W., Liu, L., Bookhagen, B., Chen, J., Tangh, J., Thompson Jobe, J.A., Li, T., and Yang, H.L., 2017b, Variations of lateral bedrock erosion rates control planation of uplifting folds in the foreland of the Tian Shan, NW China: Journal of Geophysical Research–Earth Surface, v. 122, p. 2431–2467, https://doi.org/10.1002/2016JF004099.

Burbank, D.W., Puigdefàbregas, C., and Munoz, J.A., 1992, The chronology of the Eocene tectonic and stratigraphic development of the eastern Pyrenean foreland basin, northeast Spain: Geological Society of America Bulletin, v. 104, p. 1101–1120, https://doi.org/10.1130/0016-7606(1992)104<1101:TCOTET>2.3.CO;2.

Burtman, V.S., and Molnar, P., 1993, Geological and Geophysical Evidence for Deep Subduction of Continental Crust Beneath the Pamir: Geological Society of America Special Paper 281, 76 p., https://doi.org/10.1130/SPE281-p1.

Butler, R.F., Lindsay, E.H., Jacobs, L.L., and Johnson, N.M., 1977, Magnetostratigraphy of the Cretaceous-Tertiary boundary in the San Juan Basin, New Mexico: Nature, v. 267, p. 318–323, https://doi.org/10.1038/267318a0.

Cao, K., Bernet, M., Wang, G.-C., van der Beek, P., Wang, A., Zhang, K.-X., and Enkelmann, E., 2013, Focused Pliocene–Quaternary exhumation of the Eastern Pamir domes, western China: Earth and Planetary Science Letters, v. 363, p. 16–26, https://doi.org/10.1016/j.epsl.2012.12.023.

Charreau, J., Gumiaux, C., Avouac, J.-P., Augier, R., Chen, Y., Barrier, L., Gilder, S., Dominguez, S., Charles, N., and Wang, Q., 2009, The Neogene Xiyu Formation, a diachronous prograding gravel wedge at the front of the Tianshan: Climatic and tectonic implications: Earth and Planetary Science Letters, v. 287, p. 298–310, https://doi.org/10.1016/j.epsl.2009.07.035.

Chen, H.L., Zhang, F.F., Cheng, X.G., Liao, L., Luo, J.C., Shi, J., Wang, B.Q., Yang, C.F., and Chen, L.F., 2010, The deformation features and basin-range coupling structure in the northeastern Pamir tectonic belt: Chinese Journal of Geology, v. 45, p. 102–112.

Chen, J., Burbank, D.W., Scharer, K.M., Sobel, E., Yin, J., Rubin, C., and Zhao, R., 2002, Magnetochronology of the Upper Cenozoic strata in the southwestern Chinese Tian Shan: Rates of Pleistocene folding and thrusting: Earth and Planetary Science Letters, v. 195, p. 113–130, https://doi.org/10.1016/S0012-821X(01)00579-9.

Chen, J., Scharer, K.M., Burbank, D.W., Heermance, R., and Wang, C.S., 2005, Quaternary detachment folding of the Mingyaole anticline, southwestern Tianshan: Dizhen Dizhi, v. 27, p. 530–547 [in Chinese].

Chen, J., Heermance, R., Burbank, D.W., Scharer, K.M., Miao, J., and Wang, C., 2007, Quantification of growth and lateral propagation of the Kashi anticline, southwest Chinese Tian Shan: Journal of Geophysical Research, v. 112, B03S16, https://doi.org/10.1029/2006JB004345.

Chen, X., Chen, H., Cheng, X., Shen, Z., and Lin, X., 2015, Sedimentology and magnetostratigraphy of the Tierekesazi Cenozoic section in the foreland region of south West Tian Shan in western China: Tectonophysics, v. 654, p. 156–172, https://doi.org/10.1016/j.tecto.2015.05.009.

Cheng, X., Chen, H., Lin, X., Yang, S., Chen, S., Zhang, F., Li, K., and Liu, Z., 2016, Deformation geometry and timing of the Wupoer thrust belt in the NE Pamir and its tectonic implications: Frontiers of Earth Science, v. 10, p. 751–760, https://doi.org/10.1007/s11707-016-0606-z.

Chmeleff, J., von Blanckenburg, F., Kossert, K., and Jakob, D., 2010, Determination of the 10Be half-life by multicollector ICP-MS and liquid scintillation counting: Nuclear Instruments & Methods in Physics Research, Section B, Beam Interactions with Materials and Atoms, v. 268, p. 192–199, https://doi.org/10.1016/j.nimb.2009.09.012.

Ciampalini, A., Persano, C., Fabel, D., and Firpo, M., 2015, Dating Pleistocene deltaic deposits using in-situ 26Al and 10Be cosmogenic nuclides: Quaternary Geochronology, v. 28, p. 71–79, https://doi.org/10.1016/j.quageo.2015.04.005.

Coutand, I., Strecker, M.R., Arrowsmith, J.R., Hilley, G., Thiede, R.C., Korjenkov, A., and Omuraliev, M., 2002, Late Cenozoic tectonic development of the intramontane Alai Valley, (Pamir–Tien Shan region, Central Asia): An example of intracontinental deformation due to the Indo-Eurasia collision: Tectonics, v. 21, no. 6, 1053, https://doi.org/10.1029/2002TC001358.

Craddock, W.H., Kirby, E., Harkins, N.W., Zhang, H., Shi, X., and Liu, J., 2010, Rapid fluvial incision along the Yellow River during headward basin integration: Nature Geoscience, v. 3, p. 209–213, https://doi.org/10.1038/ngeo777.

Dahlen, F.A., 1990, Critical taper model of fold-and-thrust belts and accretionary wedges: Annual Review of Earth and Planetary Sciences, v. 18, p. 55–99, https://doi.org/10.1146/annurev.ea.18.050190.000415.

Dahlen, F.A., Suppe, J., and Davis, D., 1984, Mechanics of fold-and-thrust belts and accretionary wedges: Cohesive Coulomb theory: Journal of Geophysical Research–Solid Earth, v. 89, p. 10,087–10,101, https://doi.org/10.1029/JB089iB12p10087.

Davis, D., Suppe, J., and Dahlen, F.A., 1983, Mechanics of fold-and-thrust belts and accretionary wedges: Journal of Geophysical Research, v. 88, p. 1153–1172, https://doi.org/10.1029/JB088iB02p01153.

Davis, M., Matmon, A., Fink, D., Ron, H., and Niedermann, S., 2011, Dating Pliocene lacustrine sediments in the central Jordan Valley, Israel—Implications for cosmogenic burial dating: Earth and Planetary Science Letters, v. 305, p. 317–327, https://doi.org/10.1016/j.epsl.2011.03.003.

Dorr, J.A., Jr., Spearing, D.R., and Steidtmann, J.R., 1977, The tectonic and synorogenic depositional history of the Hoback basin and adjacent areas, in Heisey, E.L., et al., eds., Rocky Mountain Thrust Belt Geology and Resources; 29th Annual Field Conference Guidebook: Casper, Wyoming, Wyoming Geological Association, p. 549–562.

Ensley, R.A., and Verosub, K.L., 1982, A magnetostratigraphic study of the sediments of the Ridge Basin, southern California, and its tectonic and sedimentologic implications: Earth and Planetary Science Letters, v. 59, p. 192–207, https://doi.org/10.1016/0012-821X(82)90125-X.

Erlanger, E.D., Granger, D.E., and Gibbon, R.J., 2012, Rock uplift rates in South Africa from isochron burial dating of fluvial and marine terraces: Geology, v. 40, p. 1019–1022, https://doi.org/10.1130/G33172.1.

Gao, R., Hou, H., Cai, X., Knapp, J.H., He, R., Liu, J., Xiong, X., Guan, Y., Li, W., Zeng, L., and Roecker, S.W., 2013, Fine crustal structure beneath the junction of the southwest Tian Shan and Tarim Basin, NW China: Lithosphere, v. 5, p. 382–392, https://doi.org/10.1130/L248.1.

Granger, D.E., and Muzikar, P.F., 2001, Dating sediment burial with in situ–produced cosmogenic nuclides: Theory, techniques, and limitations: Earth and Planetary Science Letters, v. 188, p. 269–281, https://doi.org/10.1016/S0012-821X(01)00309-0.

Granger, D.E., Kirchner, J.W., and Finkel, R.C., 1997, Quaternary downcutting rate of the New River, Virginia, measured from differential decay of cosmogenic 26Al and 10Be in cave-deposited alluvium: Geology, v. 25, p. 107–110, https://doi.org/10.1130/0091-7613(1997)025<0107:QDROTN>2.3.CO;2.

Gunderson, K.L., Pazzaglia, F.J., Picotti, V., Anastasio, D.A., Kodama, K.P., Rittenour, T., Frankel, K.F., Ponza, A., Berti, C., Negri, A., et al., 2014, Unraveling tectonic and climatic controls on synorogenic growth strata (Northern Apennines, Italy): Geological Society of America Bulletin, v. 126, p. 532–552, https://doi.org/10.1130/B30902.1.

Gutscher, M.-A., Kukowski, N., Malavieille, J., and Lallemand, S., 1996, Cyclical behavior of thrust wedges: Insights from high basal friction sandbox experiments: Geology, v. 24, p. 135–138, https://doi.org/10.1130/0091-7613(1996)024<0135:CBOTWI>2.3.CO;2.

Heermance, R.V., Chen, J., Burbank, D.W., and Wang, C., 2007, Chronology and tectonic controls of Late Tertiary deposition in the southwestern Tian Shan foreland, NW China: Basin Research, v. 19, p. 599–632, https://doi.org/10.1111/j.1365-2117.2007.00339.x.

Heermance, R.V., Chen, J., Burbank, D.W., and Miao, J., 2008, Temporal constraints and pulsed late Cenozoic deformation during the structural disruption of the active Kashi foreland, northwest China: Tectonics, v. 27, TC6012, https://doi.org/10.1029/2007TC002226.

Ischuk, A., Bendick, R., Rybin, A., Molnar, P., Khan, S.F., Kuzikov, S., Mohadjer, S., Saydullaev, U., Ilyasova, Z., Schelochkov, G., and Zubovich, A.V., 2013, Kinematics of the Pamir and Hindu Kush regions from GPS geodesy: Journal of Geophysical Research–Solid Earth, v. 118, p. 2408–2416, https://doi.org/10.1002/jgrb.50185.

Kong, P., Zheng, Y., and Fu, B., 2011, Cosmogenic nuclide burial ages and provenance of late Cenozoic deposits in the Sichuan Basin: Implications for early Quaternary glaciations in east Tibet: Quaternary Geochronology, v. 6, p. 304–312, https://doi.org/10.1016/j.quageo.2011.03.006.

Lal, D., 1991, Cosmic ray labeling of erosion surfaces: In situ nuclide production rates and erosion models: Earth and Planetary Science Letters, v. 104, p. 424–439, https://doi.org/10.1016/0012-821X(91)90220-C.

Li, T., Chen, J., Thompson, J.A., Burbank, D.W., and Xiao, W., 2012, Equivalency of geologic and geodetic rates in contractional orogens: New insights from the Pamir Frontal thrust: Geophysical Research Letters, v. 39, L15305, https://doi.org/10.1029/2012GL051782.

Li, T., Chen, J., Thompson, J.A., Burbank, D.W., and Yang, X., 2013, Quantification of three-dimensional folding using fluvial terraces: A case study from the Mushi anticline, northern margin of the Chinese Pamir: Journal of Geophysical Research–Solid Earth, v. 118, p. 4628–4647, https://doi.org/10.1002/jgrb.50316.

Li, T., Chen, J., Thompson, J.A., Burbank, D.W., and Yang, X., 2015a, Active flexural-slip faulting: A study from the Pamir–Tian Shan convergent zone, NW China: Journal of Geophysical Research–Solid Earth, v. 120, p. 4359–4378, https://doi.org/10.1002/2014JB011632.

Li, T., Chen, J., Thompson, J.A., Burbank, D.W., and Yang, H., 2015b, Hinge-migrated fold-scarp model based on an analysis of bed geometry: A study from the Mingyaole anticline, southern foreland of Chinese Tian Shan: Journal of Geophysical Research–Solid Earth, v. 120, p. 6592–6613, https://doi.org/10.1002/2015JB012102.

Liu, D., Li, H., Sun, Z., Cao, Y., Wang, L., Pan, J., Han, L., and Ye, X., 2017, Cenozoic episodic uplift and kinematic evolution between the Pamir and southwestern Tien Shan: Tectonophysics, v. 712–713, p. 438–454, https://doi.org/10.1016/j.tecto.2017.06.009.

Liu, X., Shen, G., Tu, H., Lu, C., and Granger, D.E., 2015, Initial 26Al/10Be burial dating of the hominin site, Bailong Cave in Hubei Province, central China: Quaternary International, v. 389, p. 235–240, https://doi.org/10.1016/j.quaint.2014.10.028.

Matmon, A., Fink, D., Davis, M., Niedermann, S., Rood, D., and Frumkin, A., 2014, Unraveling rift margin evolution and escarpment development ages along the Dead Sea fault using cosmogenic burial ages: Quaternary Research, v. 82, p. 281–295, https://doi.org/10.1016/j.yqres.2014.04.008.

Matmon, A., Stock, G.M., Granger, D.E., and Howard, K.A., 2012, Dating of Pliocene Colorado River sediments: Implications for cosmogenic burial dating and the evolution of the lower Colorado River: Geological Society of America Bulletin, v. 124, p. 626–640, https://doi.org/10.1130/B30453.1.

McPhillips, D., Hoke, G.D., Liu-Zeng, J., Bierman, P.R., Rood, D.H., and Niedermann, S., 2016, Dating the incision of the Yangtze River gorge at the First Bend using three-nuclide burial ages: Geophysical Research Letters, v. 43, p. 101–110, https://doi.org/10.1002/2015GL066780.

Muzikar, P., and Granger, D., 2006, Combining cosmogenic, stratigraphic, and paleomagnetic information using a Bayesian approach: General results and an application to Sterkfontein: Earth and Planetary Science Letters, v. 243, p. 400–408.

Naylor, M., and Sinclair, H.D., 2007, Punctuated thrust deformation in the context of doubly vergent thrust wedges: Implications for the localization of uplift and exhumation: Geology, v. 35, p. 559–562, https://doi.org/10.1130/G23448A.1.

Negredo, A.M., Replumaz, A., Villaseñor, A., and Guillot, S., 2007, Modeling the evolution of continental subduction processes in the Pamir–Hindu Kush region: Earth and Planetary Science Letters, v. 259, p. 212–225, https://doi.org/10.1016/j.epsl.2007.04.043.

Nishiizumi, K., 2004, Preparation of 26Al AMS standards: Nuclear Instruments & Methods in Physics Research, Section B, Beam Interactions with Materials and Atoms, v. 223–224, p. 388–392, https://doi.org/10.1016/j.nimb.2004.04.075.

Nishiizumi, K., Winterer, E.L., Kohl, C.P., Klein, J., Middleton, R., Lal, D., and Arnold, J.R., 1989, Cosmic ray production rates of ^{10}Be and ^{26}Al in quartz from glacially polished rocks: Journal of Geophysical Research–Solid Earth, v. 94, p. 17,907–17,915, https://doi.org/10.1029/JB094iB12p17907.

Nishiizumi, K., Imamura, M., Caffee, M.W., Southon, J.R., Finkel, R.C., and McAninch, J., 2007, Absolute calibration of ^{10}Be AMS standards, Nuclear Instruments and Methods in Physics Research Section B: Beam Interactions with Materials and Atoms, v. 258, no. 2, p. 403–413.

Norris, T.L., Gancarz, A.J., Rokop, D.J., and Thomas, K.W., 1983, Half-life of ^{26}Al: Journal of Geophysical Research–Solid Earth, v. 88, p. B331–B333, https://doi.org/10.1029/JB088iS01p0B331.

Ogg, J.G., 2012, Geomagnetic polarity time scale, in Gradstein, F.M., Ogg, J.G., Schmitz, M.D., and Ogg, G., eds., The Geologic Time Scale: Amsterdam, Netherlands, Elsevier, p. 85–113, https://doi.org/10.1016/B978-0-444-59425-9.00005-6.

Pavlis, T.L., Hamburger, M.W., and Pavlis, G.L., 1997, Erosional processes as a control on the structural evolution of an actively deforming fold and thrust belt: An example from the Pamir–Tien Shan region, Central Asia: Tectonics, v. 16, p. 810–822, https://doi.org/10.1029/97TC01414.

Platt, J.P., 1988, The mechanics of frontal imbrication: A first-order analysis: Geologische Rundschau, v. 77, p. 577–589, https://doi.org/10.1007/BF01832399.

Poblet, J., McClay, K., Storti, F., and Munoz, J.A., 1997, Geometries of syntectonic sediments associated with single-layer detachment folds: Journal of Structural Geology, v. 19, p. 369–381, https://doi.org/10.1016/S0191-8141(96)00113-7.

Puchol, N., Charreau, J., Blard, P-H., Lavé, J., Dominguez, S., Pik, R., Saint-Carlier, D., and the ASTER Team, 2017, Limited impact of Quaternary glaciations on denudation rates in Central Asia: Geological Society of America Bulletin, v. 129, p. 479–499, https://doi.org/10.1130/B31475.1.

Qiao, Q., Huang, B., Piper, J.D.A., Deng, T., and Liu, C., 2016, Neogene magnetostratigraphy and rock magnetic study of the Kashi Depression, NW China: Implications to neotectonics in the SW Tianshan Mountains: Journal of Geophysical Research–Solid Earth, v. 121, p. 1280–1296, https://doi.org/10.1002/2015JB012687.

Qiao, Q., Huang, B., Biggin, A.J., and Piper, J.D.A., 2017, Late Cenozoic evolution in the Pamir–Tian Shan convergence: New chronological constraints from the magnetostratigraphic record of the southwestern Tianshan foreland basin (Ulugqat area): Tectonophysics, v. 717, p. 51–64, https://doi.org/10.1016/j.tecto.2017.07.013.

Riba, O., 1976, Syntectonic unconformities of the Alto Cardener, Spanish Pyrenees: A genetic interpretation: Sedimentary Geology, v. 15, p. 213–233, https://doi.org/10.1016/0037-0738(76)90017-8.

Rutte, D., Ratschbacher, L., Khan, J., Stübner, K., Hacker, B.R., Stearns, M.A., Enkelmann, E., Jonckheere, R., Pfänder, J.A., Sperner, B., and Tichomirowa, M., 2017, Building the Pamir-Tibetan Plateau—Crustal stacking, extensional collapse, and lateral extrusion in the Central Pamir: 2. Timing and rates: Tectonics, v. 36, p. 385–419, https://doi.org/10.1002/2016TC004294.

Scharer, K.M., Burbank, D.W., Chen, J., Weldon, R.J., Rubin, C., Zhao, R., and Shen, J., 2004, Detachment folding in the southwestern Tian Shan–Tarim foreland, China: Shortening estimates and rates: Journal of Structural Geology, v. 26, p. 2119–2137, https://doi.org/10.1016/j.jsg.2004.02.016.

Scharer, K.M., Burbank, D.W., Chen, J., and Weldon, R.J., 2006, Kinematic models of fluvial terraces over active detachment folds: Constraints on the growth mechanism of the Kashi-Atushi fold system, Chinese Tian Shan: Geological Society of America Bulletin, v. 118, p. 1006–1021, https://doi.org/10.1130/B25835.1.

Schmidt, J., Hacker, B.R., Ratschbacher, L., Stübner, K., Stearns, M., Kylander-Clark, A., Cottle, J.M., Webb, A.A.G., Gehrels, G., and Minaev, V., 2011, Cenozoic deep crust in the Pamir: Earth and Planetary Science Letters, v. 312, p. 411–421, https://doi.org/10.1016/j.epsl.2011.10.034.

Schneider, F.M., Yuan, X., Schurr, B., Mechie, J., Sippl, C., Haberland, C., Minaev, V., Oimahmadov, I., Gadoev, M., Radjabov, N., Abdybachaev, U., Orunbaev, S., and Negmatullaev, S., 2013, Seismic imaging of subducting continental lower crust beneath the Pamir: Earth and Planetary Science Letters, v. 375, p. 101–112, https://doi.org/10.1016/j.epsl.2013.05.015.

Shang, X.L., Chen, X.W., Wu, C., and Luo, J.H., 2004, Cenozoic thrust structures in the Kashi Area, western Tarim Basin: Chinese Journal of Geology, v. 39, no. 4, p. 543–550 (in Chinese with English abstract).

Sobel, E.R., and Dumitru, T.A., 1997, Exhumation of the margins of the western Tarim Basin during the Himalayan orogeny: Journal of Geophysical Research, v. 102, p. 5043–5063, https://doi.org/10.1029/96JB03267.

Sobel, E.R., Chen, J., and Heermance, R., 2006, Late Oligocene–early Miocene initiation of shortening in the southwestern Chinese Tian Shan: Implications for Neogene shortening rate variations: Earth and Planetary Science Letters, v. 247, p. 70–81, https://doi.org/10.1016/j.epsl.2006.03.048.

Sobel, E.R., Schoenbohm, L.M., Chen, J., Thiede, R., Stockli, D.F., Sudo, M., and Strecker, M.R., 2011, Late Miocene–Pliocene deceleration of dextral slip between Pamir and Tarim: Implications for Pamir orogenesis: Earth and Planetary Science Letters, v. 304, p. 369–378, https://doi.org/10.1016/j.epsl.2011.02.012.

Sobel, E.R., Chen, J., Schoenbohm, L.M., Thiede, R., Stockli, D.F., Sudo, M., and Strecker, M.R., 2013, Oceanic-style subduction controls late Cenozoic deformation of the Northern Pamir orogen: Earth and Planetary Science Letters, v. 363, p. 204–218, https://doi.org/10.1016/j.epsl.2012.12.009.

Stearns, M.A., Hacker, B.R., Ratschbacher, L., Rutte, D., and Kylander-Clark, A.R.C., 2015, Titanite petrochronology of the Pamir gneiss domes: Implications for middle to deep crust exhumation and titanite closure to Pb and Zr diffusion: Tectonics, v. 34, p. 784–802, https://doi.org/10.1002/2014TC003774.

Stock, G.M., Anderson, R.S., and Finkel, R.C., 2004, Pace of landscape evolution in the Sierra Nevada, California, revealed by cosmogenic dating of cave sediments: Geology, v. 32, p. 193–196, https://doi.org/10.1130/G20197.1.

Stone, J.O., 2000, Air pressure and cosmogenic isotope production: Journal of Geophysical Research, v. 105, p. 23,753–23,759, https://doi.org/10.1029/2000JB900181.

Strecker, M.R., Frisch, W., Hamburger, M.W., Ratschbacher, L., Semiletkin, S., Zamoruyev, A., and Sturchio, N., 1995, Quaternary deformation in the Eastern Pamirs, Tadzhikistan and Kyrgyzstan: Tectonics, v. 14, p. 1061–1079, https://doi.org/10.1029/95TC00927.

Suppe, J., Chou, G.T., and Hook, S.C., 1992, Rates of folding and faulting determined from growth strata, in McClay, K.R., ed., Thrust Tectonics: London, Chapman and Hall, p. 102–121.

Talling, P.J., Lawton, T.F., Burbank, D.W., and Hobbs, R.S., 1995, Evolution of latest Cretaceous–Eocene nonmarine deposystems in the Axhandle piggyback basin of central Utah: Geological Society of America Bulletin, v. 107, p. 297–315, https://doi.org/10.1130/0016-7606(1995)107<0297:EOLCEN>2.3.CO;2.

Tang, Z., Dong, X., Wang, X., and Ding, Z., 2015, Oligocene–Miocene magnetostratigraphy and magnetic anisotropy of the Baxbulak section from the Pamir–Tian Shan convergence zone: Geochemistry Geophysics Geosystems, v. 16, p. 3575–3592, https://doi.org/10.1002/2015GC005965.

Thompson, J.A., 2013, Neogene Tectonic Evolution of the NE Pamir Margin, NW China [Ph.D. dissertation]: University of California Santa Barbara, 257 p.

Thompson, J.A., Burbank, D.W., Li, T., Chen, J., and Bookhagen, B., 2015, Late Miocene northward propagation of the northeast Pamir thrust system, northwest China: Tectonics, v. 34, p. 510–534, https://doi.org/10.1002/2014TC003690.

Thompson, J.A., Chen, J., Yang, H.L., Li, T., Bookhagen, B., and Burbank, D.W., 2018, Coarse-versus fine-grain quartz OSL and cosmogenic ^{10}Be-dating of deformed fluvial terraces on the northeast Pamir margin, northwest China: Quaternary Geochronology, v. 46, p. 1–15, https://doi.org/10.1016/j.quageo.2018.01.002.

Thompson Jobe, J.A., Li, T., Burbank, D.W., Chen, J., and Bufe, A., 2017, Quaternary tectonics of the Pamir–Tian Shan convergence zone, NW China: Tectonics, v. 36, p. 2748–2776, https://doi.org/10.1002/2017TC004541.

Tofelde, S., Schildgen, T.F., Savi, S., Pingel, H., Wickert, A.D., Bookhagen, B., Wittmann, H., Alonso, R.N., Cottle, J., and Strecker, M.R., 2017, 100 kyr fluvial cut-and-fill terrace cycles since the middle Pleistocene in the southern Central Andes, NW Argentina: Earth and Planetary Science Letters, v. 473, p. 141–153, https://doi.org/10.1016/j.epsl.2017.06.001.

Tu, H., Shen, G., Li, H., Xie, F., and Granger, D.E., 2015, ^{26}Al/^{10}Be burial dating of Xujiayao-Houjiayao site in Nihewan Basin, northern China: PLOS One, v. 10, p. e0118315, https://doi.org/10.1371/journal.pone.0118315.

Vermeesch, P., Fenton, C.R., Kober, F., Wiggs, G.F.S., Bristow, C.S., and Xu, S., 2010, Sand residence times of one million years in the Namib Sand Sea from cosmogenic nuclides: Nature Geoscience, v. 3, p. 862–865, https://doi.org/10.1038/ngeo985.

Wang, C., Cheng, X., Chen, H., Ding, W., Lin, X., Wu, L., Li, K., Shi, J., and Li, Y., 2016, The effect of foreland palaeo-uplift on deformation mechanism in the Wupoer fold-and-thrust belt, NE Pamir: Constraints from analogue modelling: Journal of Geodynamics, v. 100, p. 115–129, https://doi.org/10.1016/j.jog.2016.03.001.

Wittmann, H., Von Blanckenburg, F., Maurice, L., Guyot, J.-L., and Kubik, P.W., 2011, Recycling of Amazon floodplain sediment quantified by cosmogenic ^{26}Al and ^{10}Be: Geology, v. 39, p. 467–470, https://doi.org/10.1130/G31829.1.

Wolkowinsky, A.J., and Granger, D.E., 2004, Early Pleistocene incision of the San Juan River, Utah, dated with ^{26}Al and ^{10}Be: Geology, v. 32, p. 749–752, https://doi.org/10.1130/G20541.1.

Xinjiang Bureau of Geology and Mineral Resources, 1993, Regional Geology of the Xinjiang Uygur Autonomous Region: Beijing, China, Geological Publishing House, 561 p.

Yang, W., Jolivet, M., Dupont-Nivet, G., and Guo, Z., 2014, Mesozoic–Cenozoic tectonic evolution of southwestern Tian Shan: Evidence from detrital zircon U/Pb and apatite fission track ages of the Ulugqat area, Northwest China: Gondwana Research, v. 26, p. 986–1008, https://doi.org/10.1016/j.gr.2013.07.020.

Zhang, H., Zhang, P., Champagnac, J.-D., Molnar, P., Anderson, R.S., Kirby, E., Craddock, W.H., and Liu, S., 2014, Pleistocene drainage reorganization driven by the isostatic response to deep incision into the northeastern Tibetan Plateau: Geology, v. 42, p. 303–306, https://doi.org/10.1130/G35115.1.

Zubovich, A., Schöne, T., Metzger, S., Mosienko, O., Mukhamediev, S., Sharshebaev, A., and Zech, C., 2016, Tectonic interaction between the Pamir and Tien Shan observed by GPS: Tectonics, v. 35, p. 283–292, https://doi.org/10.1002/2015TC004055.

Zubovich, A.V., et al., 2010, GPS velocity field for the Tien Shan and surrounding regions: Tectonics, v. 29, TC6014, https://doi.org/10.1029/2010TC002772.